

Theoretical Study of Ground- and Excited-State Charge Transfer in Fulvene-Based Donor-Acceptor Systems

Michal Kochman and Bo Durbeej

The self-archived postprint version of this journal article is available at Linköping University Institutional Repository (DiVA):

<http://urn.kb.se/resolve?urn=urn:nbn:se:liu:diva-159198>

N.B.: When citing this work, cite the original publication.

Kochman, M., Durbeej, Bo, (2019), Theoretical Study of Ground- and Excited-State Charge Transfer in Fulvene-Based Donor-Acceptor Systems, *Journal of Physical Chemistry A*, 123(31), 6660-6673.
<https://doi.org/10.1021/acs.jpca.9b02962>

Original publication available at:

<https://doi.org/10.1021/acs.jpca.9b02962>

Copyright: American Chemical Society

<http://pubs.acs.org/>



A Theoretical Study of Ground- and Excited-State Charge Transfer in Fulvene-Based Donor-Acceptor Systems

Michał Andrzej Kochman* and Bo Durbeej*

*Division of Theoretical Chemistry, Department of Physics, Chemistry and Biology (IFM),
Linköping University, 581 83 Linköping, Sweden.*

E-mail: michal.kochman@liu.se; bodur@ifm.liu.se

Abstract

Donor-acceptor systems based on fulvene as the electron-accepting moiety are typified by exotic, strongly polar electronic structures. In this contribution, *ab initio* calculations have been performed to explore the ground- and excited-state properties of an archetypal compound of this class, which incorporates the exocyclic carbon atom of fulvene into a tetramethylimidazoline-like five-membered ring. In the electronic ground state, the compound under study has pronounced zwitterionic character, and is best described as consisting of a negatively charged cyclopentadienyl ring linked covalently to a positively charged tetramethylimidazolium ring. Both of these rings can be considered as aromatic. The excess negative charge localized on the cyclopentadienyl ring is highly labile in the photochemical sense: the low-lying valence excited states exhibit varying degrees of reverse charge transfer, whereby electron density is transferred from the cyclopentadienyl ring back onto the tetramethylimidazolium ring. The topographies of the excited-state potential energy surfaces favor rapid and efficient internal conversion

at an extended, fulvene-like S_1/S_0 conical intersection seam. As a consequence, the excited-state lifetime of this compound is predicted to be on the order of 100 fs.

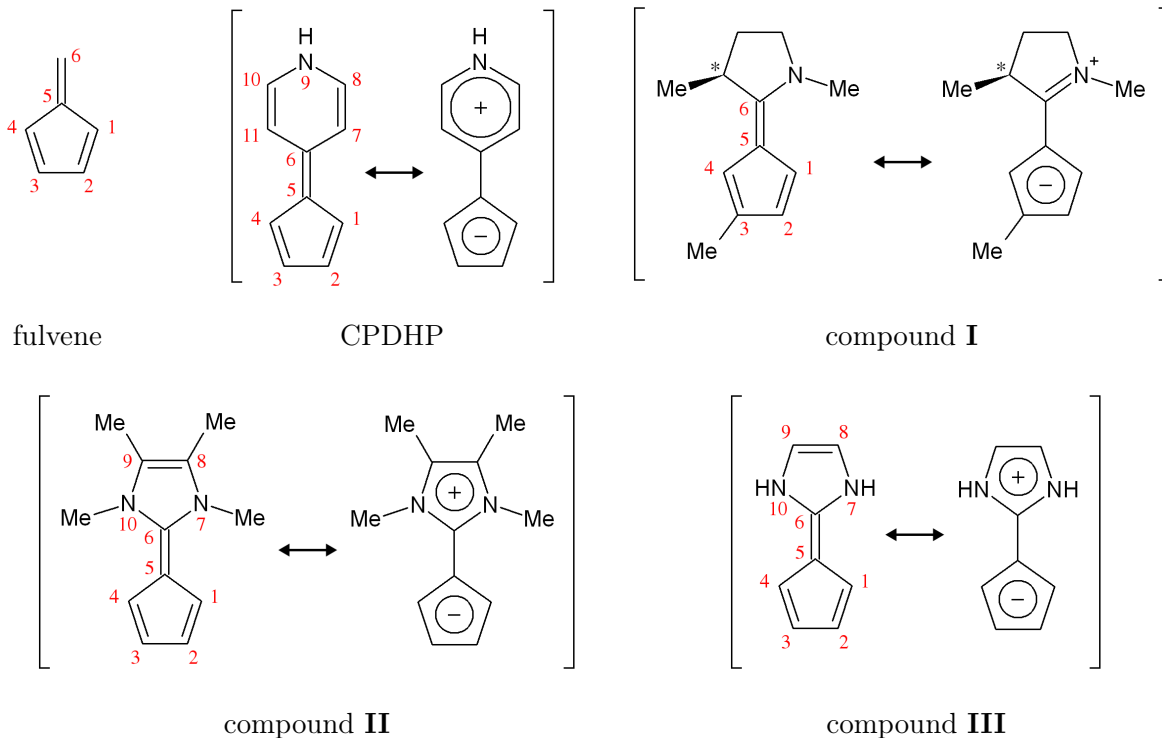
1 Introduction

The relatively simple molecular structure of the hydrocarbon fulvene (see Figure 1 for molecular structure), belies a rich and complex chemistry which has long held the attention of experimental and theoretical investigators alike. Part of the interest in fulvene as a building block in molecular design comes from its excellent electron-accepting ability. As early as 1970, Hartke and Salamon^{1,2} demonstrated that upon the substitution of position C6 with electron-donating groups, as in 6,6-diaminofulvenes, the fulvene moiety acquires a net negative charge and takes on a partial aromatic character, in resemblance to the cyclopentadienyl anion. In the language of valence bond theory, the increase in aromatic character upon substitution with electron-donating groups at the exocyclic carbon atom C6 can be described as proaromaticity: the electronic wavefunction has significant contributions from aromatized zwitterionic resonance structures.³

In one of the earliest theoretical investigations of this class of compounds, Jarjis and Khalil⁴ performed a systematic study of substituent effects on the structure and properties of fulvene derivatives. Importantly, it was determined that among the sites available for substitution, atom C6 is the most responsive to substitution with electron-donating groups.⁴ The problem of the electronic structure of fulvene derivatives was taken up in several subsequent theoretical studies.⁵⁻¹¹ The composite picture, arising from the application of a range of aromaticity indices, is that of increased aromatic character with increasing electron-donating ability of the substituent at atom C6.

The unusual, highly polar ground-state electronic structures of C6-substituted fulvene systems create the potential for interesting photophysical behavior. To date, several groups have reported the synthesis and spectroscopic characterization of fulvene-based

Figure 1: Molecular structures of fulvene, 4-cyclopentadienylidene-1,4-dihydropyridine (CPDHP) and compounds **I**, **II**, and **III**. In the Lewis structure of compound **I**, the asymmetric carbon atom is marked with an asterisk.



donor-acceptor chromophores.^{12–17} There have also been some efforts to investigate the optical properties of systems of this type with the use of electronic structure calculations. Notably, Haas and coworkers^{18–20} have studied the excited-state relaxation mechanism of the compound 4-cyclopentadienylidene-1,4-dihydropyridine^{21–23} (CPDHP, see Figure 1), which incorporates fulvene’s atom C6 into a pyridinium-like six-membered ring. These authors demonstrated the existence of a conical intersection between the ground electronic state and an excited state of A symmetry, located at a geometry where the five- and six-membered rings adopt a perpendicular orientation.^{18–20} It was furthermore predicted that following photoexcitation, CPDHP undergoes a full rotation around the central C=C bond connecting the two rings, in the process encountering the conical intersection seam and deactivating to the electronic ground state.^{19,20} In principle, such an intramolecular rotation process

provides a basis for the application of CPDHP as a light-operated molecular switch: a molecule which can be reversibly shifted between *E* and *Z* isomeric forms by irradiation in the ultraviolet-visible range of the electromagnetic spectrum.

Independently, Oruganti et al.^{24,25} utilized the molecular skeleton of fulvene as a basis for a proposed molecular motor, denoted compound **I** in Figure 1. In this system, an asymmetric carbon atom was introduced adjacent to atom C6 in order to enforce unidirectional rotation around the central C=C bond. On the basis of nonadiabatic molecular dynamics simulations, it was predicted that this design achieves a high quantum yield of photoisomerization (ca. 75%). This finding raised the hope that substitution at position C6 could form a general strategy for the synthesis of photoswitchable molecules.

In view of the continued interest in fulvene-based donor-acceptor systems, the present study aims to construct a detailed theoretical picture of fulvene as the charge-accepting component of donor-acceptor chromophores. The focus is on the structures of the relevant electronic states, and the topography of the corresponding ground- and excited-state potential energy surfaces (PESs). We employed compound **II**, whose structure is illustrated in Figure 1, as the model system for the purposes of our simulations. This fulvene derivative was synthesized by Kunz et al.²⁶ (see also Refs.²⁷⁻²⁹) as a ligand for the synthesis of metallocene complexes; it incorporates the atom C6 of the fulvene moiety into a tetramethyl-substituted, imidazoline-like five-membered ring. We expect compound **II** to be representative of the photophysics of fulvene-based donor-acceptor compounds. At the same time, its relatively small size means that it is amenable to study with the use of high-level electronic structure methods.

The rest of the paper is organized as follows. Firstly, we outline our simulation methodology. Afterwards, we briefly review the ground-state electronic structure of the compound under study. We then move on to examine its low-lying excited electronic states and their PESs. Lastly, we characterize the excited-state relaxation process which ensues from the irradiation of its lowest photoabsorption band.

2 Computational Methods

2.1 Electronic Structure Methods

We adopted the following general strategy for the exploration of the photophysics of compound **II**. The topographies of the ground- and excited-state PESs were mapped out with the use of the complete active space self-consistent field³⁰ (CASSCF) method. In some cases, energies obtained with the CASSCF method were corrected for dynamical electron correlation in single-point calculations performed with the use of extended multi-state complete active space second-order perturbation theory³¹ (XMS-CASPT2). In the CASSCF and XMS-CASPT2 calculations, compound **II** was represented by a size-reduced model (compound **III**; see Figure 1) in which all four methyl groups are replaced with hydrogen atoms. The replacement of the methyl groups with hydrogens has only a slight effect on the electronic states of the molecule, and allows a substantial reduction of computational cost.

Except where noted otherwise, we normally employed the cc-pVDZ basis set developed by Dunning.³⁴

The CASSCF and XMS-CASPT2 calculations were performed with the program BAGEL,^{32,33} version 1.1.2. The active space consisted of 12 electrons distributed among the 10 π - and π^* -type orbitals which arise mainly from the 2p atomic orbitals of the carbon and nitrogen atoms. A state-averaging (SA) scheme was imposed. Depending on circumstances, either the lowest two (SA-2), or the lowest three (SA-3) singlet states were included, as appropriate for a given calculation. The cc-pVDZ basis set was used in combination with the default density fitting basis set from the BAGEL library. At the XMS-CASPT2 stage, the so-called SS-SR contraction scheme³⁵ was used, and the vertical shift was set to $0.2 E_h$.

In order to obtain a measure of the sensitivity of calculated excitation energies to basis set size, the vertical excitation spectrum of compound **III** was also calculated at the XMS-CASPT2 level of theory with the use of the larger cc-pVTZ basis set.

The relevant electronic states of compound **II** were also characterized (without resorting

to a size-reduced model) with the use of the Møller-Plesset perturbation method of second order (MP2) for the ground state, and the algebraic-diagrammatic construction method of second order^{36,37} (ADC(2)) for the excited states. The MP2 and ADC(2) calculations were performed within the computational chemistry software package Turbomole version 6.3.1,³⁸ taking advantage of the frozen core and resolution of the identity^{39–42} approximations. The default auxiliary basis set was used.⁴³

Lastly, nonadiabatic molecular dynamics simulations were performed in order to model the relaxation process of compound **II** triggered by irradiation near the maximum of its first photoabsorption band. These simulations also relied on the combination of MP2 and ADC(2) for the treatment of electronic structure.

All calculations reported in the main body of the present paper address only the valence-type excited states of compound **II**. Calculations performed with a diffuse-augmented basis set additionally detect a manifold of low-lying Rydberg-type excited states. As a rule, in molecular clusters and in the condensed phase, Rydberg-type excited states are destabilized with respect to valence excited states.^{44–46} In all calculations discussed in the main body of this paper, we assume a generic nonpolar condensed-phase context, in which only the valence excited states are likely to be involved in the photophysics of compound **II**. Accordingly, we focus on the structures and PESs of the valence excited states. The discussion of the Rydberg-type states is relegated to Section S2 of the Supporting Information.

Moreover, we also considered the effect of polar solvation on the photophysics of compound **II**. To this end, we carried out a separate set of simulations with the use of implicit (i.e., continuum) and explicit solvent models. Our findings in this regard are summarized in Section S4 of the Supporting Information.

2.2 Nonadiabatic Molecular Dynamics

In the nonadiabatic molecular dynamics simulations, the simultaneous evolution of the electronic and the nuclear degrees of freedom was modeled via the fewest switches surface

hopping (FSSH) method.^{47–50} The MP2 and ADC(2) combination was used for the on-the-fly calculation of energies, gradients, and nonadiabatic coupling elements.

Within the framework of the FSSH method, the nuclear wavepacket of the system is represented by an ensemble of mutually independent semiclassical trajectories. In each trajectory, the nuclear dynamics is described by means of classical mechanics, while the electrons are treated quantum-mechanically. The total wavefunction $\Phi(\mathbf{r}, t; \mathbf{R})$ of the electrons is written as a linear combination of adiabatic electronic states $\{\phi_j(\mathbf{r}; \mathbf{R})\}$ with time-dependent coefficients $\{a_j(t)\}$:

$$\Phi(\mathbf{r}, t; \mathbf{R}) = \sum_j a_j(t) \phi_j(\mathbf{r}; \mathbf{R}) \quad (1)$$

Here, \mathbf{r} denotes the electronic coordinates, and $\mathbf{R} = \mathbf{R}(t)$ is the trajectory followed by the nuclei. The requirement that $\Phi(\mathbf{r}, t; \mathbf{R})$ satisfies the time-dependent electronic Schrödinger equation leads to the following system of coupled differential equations for the time-evolution of the expansion coefficients:

$$i\hbar \dot{a}_k = \sum_j a_j (\delta_{jk} E_k(\mathbf{R}) - i\hbar C_{kj}) \quad (2)$$

where δ_{jk} denotes the Kronecker delta, $E_k(\mathbf{R})$ is the potential energy of the k -th adiabatic state, and $C_{kj} = \langle \phi_k | \frac{\partial}{\partial t} | \phi_j \rangle$ is the nonadiabatic coupling matrix element between states k and j .

In each simulated trajectory, at any time the system is considered to occupy some current adiabatic state n from among the states included in the linear expansion (1). The current state is selected according to its state population $|a_n|^2$. The nuclear dynamics is propagated according to Newton’s equations of motion on the PES of that state. Nonadiabatic effects are accounted for by allowing the system to undergo a switch (or “hop”) between the current state and another adiabatic state, which then becomes the new current state.

The FSSH simulations were performed with the use of the software package Newton-X

version 2.0,^{51–54} which contains an interface to Turbomole. Adiabatic states from S_1 to S_3 were included in the expansion (1). Due to the fact that the conventional implementation of ADC(2), based on a restricted Hartree-Fock reference determinant, does not provide a formally correct description of crossings of excited states with the ground state,^{55,56} the S_0 state was not included in the expansion (1), and internal conversion to the S_0 state was not modeled explicitly. Instead, when the energy gap between the currently occupied state and the ground state in a given simulated trajectory decreased to below a threshold of 0.25 eV, the molecule was considered to have undergone internal conversion to S_0 . At this point, the simulated trajectory was terminated. It should be emphasized that the above scheme for ending trajectories is only a rough approximation to the true mechanism of internal conversion to the S_0 state. The error introduced by this approximation is expected to be small in absolute terms, but unfortunately we have no way of knowing whether its effect is to over- or underestimate the excited-state lifetime with respect to reality.

The nuclear dynamics was propagated using the velocity Verlet integrator with a time step of 0.5 fs. Approximate nonadiabatic coupling elements were calculated with the use of the orbitals derivative scheme introduced by Ryabinkin and coworkers.⁵⁷ As per program defaults, the decoherence correction scheme of Granucci and Persico⁵⁸ was applied to the expansion coefficients $\{a_k(t)\}$. The correction constant was set to $C = 0.1 E_h$.

The initial conditions for the nonadiabatic molecular dynamics simulations were generated in such a way as to mimic the irradiation of the first absorption band of compound **II**. Firstly, the photoabsorption spectrum of compound **II** was simulated using the semiclassical nuclear ensemble method.^{59,60} This method takes as input a set of N_{pts} ground-state geometries of the molecule of interest ($\{\mathbf{R}_i\}$), which are sampled either from a statistical distribution or from thermostatted molecular dynamics trajectories. Vertical excitation energies ($\Delta E_{0n}(\mathbf{R}_i)$) and associated oscillator strengths ($f_{0n}(\mathbf{R}_i)$) are then computed at each of these geometries, from which the molecular absorption cross-section

$(\sigma(E))$ is calculated as:

$$\sigma(E) = \frac{\pi e^2 \hbar}{2 m c \varepsilon_0 n_r E} \sum_{n=1}^{N_{\text{fs}}} \frac{1}{N_{\text{pts}}} \sum_{i=1}^{N_{\text{pts}}} \Delta E_{0n}(\mathbf{R}_i) f_{0n}(\mathbf{R}_i) g_{\text{Gauss}}(E - \Delta E_{0n}(\mathbf{R}_i), \delta) \quad (3)$$

where $g_{\text{Gauss}}(E - \Delta E_{0n}(\mathbf{R}_i), \delta)$ is a normalized Gaussian line-shape function. n_r denotes the refraction index of the medium, and m is the electron rest mass.

In order to generate the spectrum, $N_{\text{fs}}=6$ excited states were calculated at each of $N_{\text{pts}}=500$ phase space points, which had been sampled from the Wigner distribution of the ground-state equilibrium geometry (S_0 -min) in the vibrational ground state. The broadening parameter in the line-shape functions was set to $\delta = 0.1$ eV, and the refraction index of the medium was set to unity.

The resulting simulated photoabsorption spectrum of compound **II** is shown in Figure 5 in Section 3.2. It can be seen that the simulated spectrum has a prominent and intense band in the range from around 3.2 to around 4.3 eV, peaking at 3.79 eV. Because our aim was to model the relaxation process resulting from irradiation near the band maximum, we chose to sample phase space points (i.e. sets of nuclear positions and velocities) in the energy interval of 3.8 ± 0.1 eV with probabilities proportional to the oscillator strength of the $S_0 \rightarrow S_n$ transition. A set of 40 phase space points were sampled in this manner, and each was used as the starting point for a single FSSH trajectory. The initial conditions generated with the use of this algorithm are described in more detail in Section 3.4.

As noted in Refs.,^{61–63} semiclassical simulations of hydrogen-rich molecules are prone to an artificial leakage of zero-point energy from the stretching modes of hydrogen-heavy atom bonds to other vibrational modes. In order to mitigate this problem, when generating the Wigner distribution we froze the sixteen highest vibrational modes, which correspond to C–H stretching modes.

The sequence of events during the simulated dynamics was followed by monitoring several variables whose definitions we will now provide. As per the usual convention, the

classical population of the j -th adiabatic state from among the states included in the linear expansion (1) is defined as the fraction of trajectories evolving in that state:

$$P_j(t) = \frac{N_j(t)}{N_{\text{trajs}}} \quad (4)$$

Once a simulation trajectory had approached the S_1/S_0 crossing seam, such that the energy gap between these states dropped to below 0.25 eV, it was discontinued. From then on, it was counted towards the fraction of trajectories occupying the S_0 state.

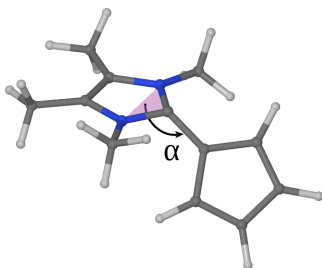
In view of the fact that the adiabatic states do not necessarily maintain their diabatic character as the molecular geometry changes, another parameter was introduced in order to track the diabatic character of the current state along the simulated trajectories. We noted that at the Franck-Condon geometry, the S_1 (2^1A) state is characterized by a high oscillator strength from S_0 , whereas the oscillator strength of the S_2 (1^1B) state is considerably lower. This suggests that the magnitude of the transition dipole moment for the transition from S_0 could form the basis for characterizing the diabatic character of the S_1 and S_2 states at other molecular geometries. Accordingly, we decided to define $\bar{\mu}_{0n}$ as the magnitude of the transition dipole moment of the currently occupied state, averaged over the ensemble of simulated trajectories:

$$\bar{\mu}_{0n} = \frac{1}{N'_{\text{trajs}}(t)} \sum_{i=1}^{N'_{\text{trajs}}(t)} \|\langle \phi_n(\mathbf{r}; \mathbf{R}_i(t)) | \hat{\boldsymbol{\mu}} | \phi_0(\mathbf{r}; \mathbf{R}_i(t)) \rangle\| \quad (5)$$

Here, $N'_{\text{trajs}}(t)$ is the number of “surviving” simulated trajectories at time t . Trajectories which had been terminated after approaching the S_1/S_0 crossing seam were excluded from the summation in equation 5.

In the S_1 (2^1A) and S_2 (1^1B) states, atom C6 has appreciable carbanionic character, and is prone to pyramidalization. This was monitored by calculating the angle α , defined as the angle formed by the C5–C6 bond, and the plane in which atoms C6, N7 and N10 lie (see Figure 2). Torsion around the central C5–C6 bond was tracked by following the value of a

Figure 2: The angle α formed by the C5–C6 bond, and the plane defined by atoms C6, N7 and N10.



parameter τ , defined as the average of the dihedral angles formed by atoms C1–C5–C6–N7, and C4–C5–C6–N10.

2.3 Analysis of Electronic Structures

As will become evident in Section 3.2, the low-lying electronic states of compound **II** involve varying degrees of intramolecular charge transfer (ICT) from the cyclopentadienyl moiety onto the tetramethylimidazolium moiety. In order to quantify the amount of charge transfer, we employed the algorithm outlined in Ref.,⁶⁴ which relies on a Voronoi-Dirichlet tessellation of space around the atomic nuclei. Namely, the parameter Δq_{TMI} was defined as the amount of electronic charge transferred into the Voronoi-Dirichlet polyhedra of nuclei belonging to the tetramethylimidazolium moiety. Furthermore, the transitions from the electronic ground state of compound **II** into its low-lying singlet excited states were also characterized by calculating the corresponding natural transition orbitals⁶⁵ (NTOs).

3 Results and Discussion

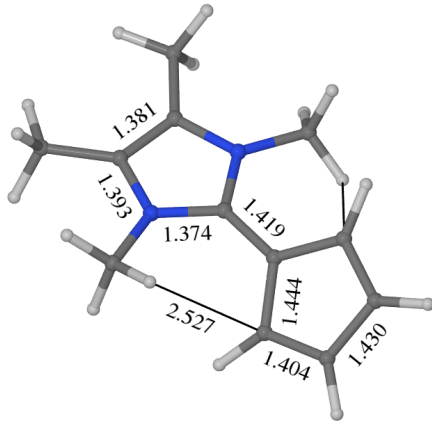
3.1 Ground Electronic State

Our first order of business will be to examine the geometric features of the electronic ground state of compound **II**. The ground-state equilibrium geometry (S_0 -min) is presented in Figure 3 (a). In agreement with the X-ray crystallographic structure determination by Kunz et al.,²⁶ we find that the cyclopentadienyl ring is twisted with respect to the tetramethylimidazolium ring around the axis formed by the central C5–C6 bond. The crystallographic geometry shows a slight breaking of C_2 symmetry,²⁶ which is presumably due to the crystalline packing. In the present calculations, however, the equilibrium geometry has ideal C_2 symmetry.

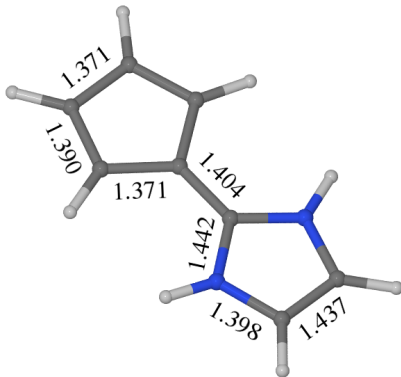
The equilibrium geometry of the model compound **III** is shown in Figure 3 (b). The replacement of the four methyl groups with hydrogen atoms reduces the steric crowding around the central C5–C6 bond, and allows compound **III** to adopt a planar ground-state equilibrium geometry. Its point group is C_{2v} .

Although the present study mainly revolves around the photophysics and excited-state properties of compound **II**, we also characterized the electronic structure and chemical bonding in its ground state. The detailed summary of our findings in this regard is relegated to Section S1 of the Supporting Information. The main result is that the ground state of compound **II** has partial zwitterionic character: the cyclopentadienyl ring bears an excess negative charge, whereas the tetramethylimidazolium moiety is positively charged. Both of the five-membered rings can be considered as aromatic.

Figure 3: Ground-state equilibrium geometries of compounds (a) **II** and (b) **III** as optimized at the MP2/cc-pVDZ level of theory. Selected bond distances are marked in units of Å. Compound **II** features charge-assisted hydrogen bonds between methyl group hydrogens, and atoms C1 and C4; see Section S1 of the Supporting Information for details.



(a) compound **II**



(b) compound **III**

3.2 Excited Electronic States

We now move on to the excited electronic states of compound **II**. The vertical excitation spectrum of compound **II** is summarized in the topmost rows of Table 1. Accompanying this data, Figure 4 provides information on the electronic structures of the low-lying excited states by plotting the NTOs for transitions from the ground state. Lastly, the simulated photoabsorption spectrum of compound **II** is plotted in Figure 5.

The lowest vertical transition is into a $\pi\pi^*$ -type state of A symmetry, which exhibits some charge transfer from the cyclopentadienyl moiety onto the tetramethylimidazolium moiety. According to the Voronoi-Dirichlet charge analysis scheme, the amount of charge transferred onto the tetramethylimidazolium moiety is $-0.193 e$. Inspection of the NTOs for the S_0 (1^1A) \rightarrow S_1 (2^1A) transition reveals that the S_1 (2^1A) state arises from the excitation of an electron from an occupied NTO localized on atom C5 and the π -bonding region of the C2–C3 bond, into a virtual NTO localized on atoms C6, N7, and N10 (see the panel on the left-hand side of Figure 4).

The S_1 (2^1A) state is closely followed by a $\pi\pi^*$ -type state of B symmetry. This

S_2 (1^1B) state is best described as an ICT state arising from the excitation of an electron from the π -bonding regions of the C1–C2 and C3–C4 bonds onto atoms C6, N7, and N10 (see the panel on the right-hand side of Figure 4). The Voronoi-Dirichlet charge analysis scheme indicates that in this state, the cyclopentadienyl moiety donates $-0.401 e$ onto the tetramethylimidazolium moiety. Thus, whereas the ground electronic state has partial zwitterionic character, the S_2 (1^1B) state is essentially nonpolar. Meanwhile, the S_1 (2^1A) state, with only a slight amount of charge transfer ($-0.193 e$) from the cyclopentadienyl moiety onto the tetramethylimidazolium moiety, falls somewhere in between the S_0 (1^1A) and S_2 (1^1B) states in terms of its polarity. Both the S_1 and S_2 states are formally ‘reverse’ ICT states. That is to say, they feature a transfer of electron density from the cyclopentadienyl moiety, which acts as the electron-accepting group in the partially zwitterionic ground state of compound **II**, onto the tetramethylimidazolium moiety.

Inspection of the dominant occupied-virtual NTO pairs for the $S_0 \rightarrow S_1$ (2^1A) and $S_0 \rightarrow S_2$ (1^1B) transitions shows that the S_1 and S_2 states are largely localized on the fulvene moiety. In terms of their electronic structures, these states are close counterparts of the lowest valence excited states of unsubstituted fulvene. One difference is that in compound **II**, the energy ordering of the A and B symmetry states is inverted with respect to fulvene, in which the A symmetry state lies well above the B symmetry state.^{66,67} We will return to the similarities between the excited states of compound **II** and those of fulvene when discussing the topography of the excited-state PES in the next section.

The oscillator strength for excitation from the ground state takes a high value of 0.541 for the S_1 (2^1A) state, but for the S_2 (1^1B) state, it is only 0.012. This latter state is a spectroscopically dark state. As a consequence, the lowest band in the photoabsorption spectrum of compound **II** (see Figure 5 (a)) arises predominantly from the 2^1A state. The dark 1^1B state does not give rise to a separate band – instead, its weak photoabsorption coalesces with that of the 2^1A state. It follows that the irradiation of the lowest photoabsorption band of compound **II** will predominantly populate the bright 2^1A state.

Only a small fraction of molecules will be excited into the dark $1\ ^1\text{B}$ state. It is expected that during the ensuing relaxation process, the $1\ ^1\text{B}$ state will become populated indirectly, via internal conversion from the initially excited $2\ ^1\text{A}$ state. This internal conversion process will be facilitated by the small energy gap between the two states at the Franck-Condon geometry.

The next-lowest valence excited state, the S_3 ($2\ ^1\text{B}$) state, is well separated in energy from the S_1 ($2\ ^1\text{A}$) and S_2 ($1\ ^1\text{B}$) states. For this reason, it is expected that this state and the higher valence excited states will not play a role in the relaxation dynamics of compound **II** following the irradiation of its lowest photoabsorption band.

Kunz and coworkers²⁶ have reported that the photoabsorption spectrum of compound **II** in dichloromethane solution features an intense band peaking at 3.67 eV, and a weak band peaking at 4.88 eV. In the simulated photoabsorption spectrum (see Figure 5 (a)), the respective band maxima are found at 3.79 eV and at 4.94 eV. The comparison of positions of the observed and calculated band maxima suggests that the ADC(2)/cc-pVDZ calculation gives rise to a slight blue shift of roughly 0.2 eV in the calculated excitation energy into the bright $2\ ^1\text{A}$ state; this level of accuracy is satisfactory for our purposes.

While on the subject of the electronic excitation spectrum of compound **II**, it is worthwhile to examine the sensitivity of calculated vertical excitation energies to the choice

Figure 4: Dominant NTOs for transitions from the S_0 ($1\ ^1\text{A}$) state into the S_1 ($2\ ^1\text{A}$) and S_2 ($1\ ^1\text{B}$) states of compound **II**, plotted in the form of isosurfaces with isovalues of $\pm 0.1\ a_0^{-3/2}$. The eigenvalue (λ_i) for each occupied-virtual NTO pair is given in terms of a percentage contribution. The calculation was performed at the ADC(2)/cc-pVDZ level of theory.

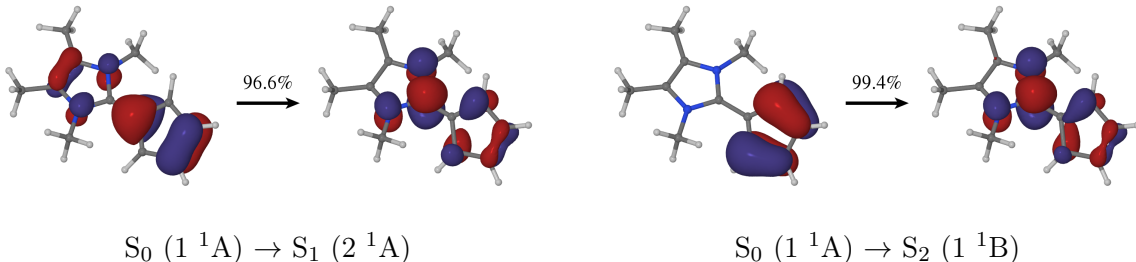
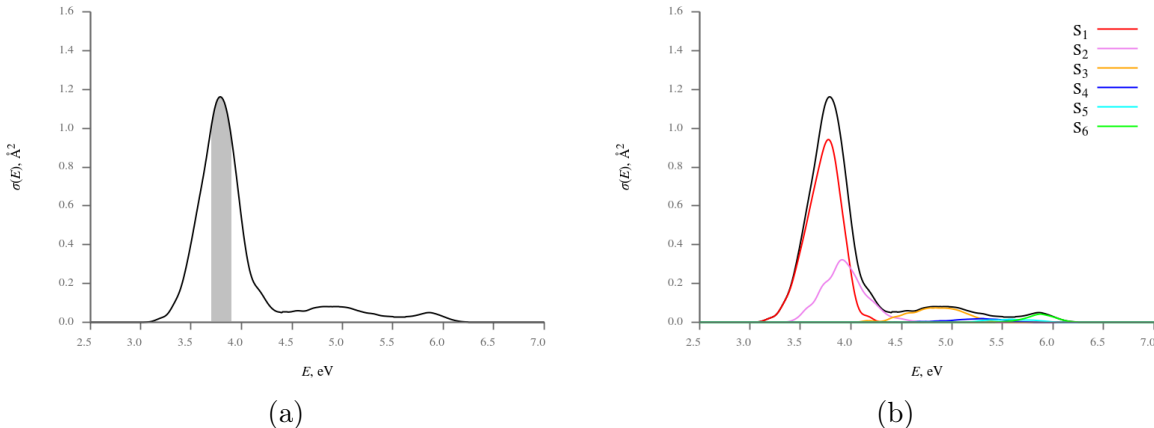


Figure 5: (a) Photoabsorption spectrum of compound **II**, simulated at the ADC(2)/cc-pVDZ level of theory. The shaded area represents the energy interval from which initial conditions for the nonadiabatic molecular dynamics simulations were sampled. (b) Breakdown of the spectrum into contributions from individual adiabatic states.



of electronic structure method and basis set. Due to the relatively large size of the molecule of compound **II**, we resort here to using compound **III** as a size-reduced model of compound **II**. Owing to the close similarity between compounds **II** and **III** and their low-lying excited states, our findings can be extrapolated to the larger compound **II**. For the sake of consistency with compound **II**, the calculation of the vertical excitation spectrum of compound **III** was performed in C_2 symmetry. In other words, when calculating the spectrum, we did not make use of the full C_{2v} symmetry of the ground-state equilibrium geometry of compound **III**.

The vertical excitation spectrum of compound **III** was calculated with the use of the ADC(2), CASSCF, and XMS-CASPT2 methods, all in combination with the cc-pVDZ basis set. In order to gain a measure of the sensitivity of calculated excitation energies to basis set size, the vertical excitation spectrum was additionally calculated at the XMS-CASPT2/cc-pVTZ level of theory.

The results of these calculations are summarized in Table 1. From a comparison of the vertical excitation spectra of compounds **II** and **III**, is immediately apparent that the lowest two singlet excited states of compound **III** are counterparts to the lowest two singlet excited states of compound **II**. More specifically, the 2^1A state of compound **III** is the counterpart

to the 2^1A state of compound **II**, and likewise for the 1^1B states of compounds **II** and **III**.

Both of the dynamically-correlated methods, ADC(2) and XMS-CASPT2, place the dark 1^1B state of compound **III** slightly higher in energy than the bright 2^1A state. In contrast, the SA-3-CASSCF calculation predicts that the 1^1B state lies vertically lower in energy than the 2^1A state. This discrepancy is attributable to the fact that the CASSCF calculation accounts for only a small amount of dynamical correlation. Otherwise, the CASSCF method is in good agreement with the dynamically-correlated methods: the 2^1A state is correctly identified as a bright state with moderate polarity, whereas the 1^1B is a dark and nonpolar state. On the basis of the above, we expect that the CASSCF method is reliable for the exploration of the ground- and excited-state PESs of compound **III**. Hence, we employed the CASSCF method for that purpose, bearing in mind that the energy ordering of the A and B symmetry states will be inverted at some molecular geometries. The results obtained with CASSCF were later verified with some additional XMS-CASPT2 calculations.

Lastly, increasing the basis set size to triple-zeta quality (cc-pVTZ) in the XMS-CASPT2 calculation causes a slight lowering of the calculated excitation energies into both the S_1 (2^1A) and the S_2 (1^1B) states, but does not alter their energy ordering. This observation indicates that the valence excited states of compound **III** are fairly insensitive to basis set size, and that a satisfactory description is achieved already with the double-zeta quality cc-pVDZ basis set.

Table 1: Vertical excitation spectra of compounds **II** and **III** calculated with the ADC(2), CASSCF, and XMS-CASPT2 methods: vertical excitation energies (ΔE) and oscillator strengths (f).

Compound	Level of theory	State	Type	ΔE , eV	f	μ , D ^a	Δq_{TMI} , e ^b
II ^c	ADC(2)/cc-pVDZ	S ₀ (1 ¹ A)				8.31 ^e	
		S ₁ (2 ¹ A)	$\pi\pi^*$	3.909	0.541	5.77	-0.193
		S ₂ (1 ¹ B)	ICT $\pi\pi^*$	4.089	0.012	2.02	-0.401
		S ₃ (2 ¹ B)	ICT $\pi\pi^*$	5.095	0.057	-2.78	-0.439
		S ₄ (3 ¹ A)	ICT $\pi\pi^*$	5.533	0.002	-5.55	-0.586
III ^c	ADC(2)/cc-pVDZ	S ₀ (1 ¹ A)				7.04 ^e	
		S ₁ (2 ¹ A)	$\pi\pi^*$	4.104	0.681	6.87	-0.068
		S ₂ (1 ¹ B)	ICT $\pi\pi^*$	4.285	0.025	2.49	-0.311
III ^c	SA-3-CASSCF/cc-pVDZ	S ₀ (1 ¹ A)				6.92	
		S ₁ (1 ¹ B)	ICT $\pi\pi^*$	4.213	0.019	5.63	
		S ₂ (2 ¹ A)	$\pi\pi^*$	4.495	0.789	1.07	
III ^c	XMS-CASPT2/cc-pVDZ	S ₀ (1 ¹ A)				7.00	
		S ₁ (2 ¹ A)	$\pi\pi^*$	3.942	0.707	5.94	
		S ₂ (1 ¹ B)	ICT $\pi\pi^*$	4.008	0.015	2.20	
III ^d	XMS-CASPT2/cc-pVTZ	S ₀ (1 ¹ A)				6.82	
		S ₁ (2 ¹ A)	$\pi\pi^*$	3.829	0.699	5.72	
		S ₂ (1 ¹ B)	ICT $\pi\pi^*$	3.941	0.015	2.22	

^a μ is the magnitude of the (orbital-relaxed) electric dipole moment of a given electronic state; a negative value indicates that its direction is antiparallel to the electric dipole moment of the S₀ state.

^b Δq_{TMI} is the amount of charge accepted by the tetramethylimidazolium fragment in a given electronic excited state, according to the Voronoi-Dirichlet spatial partitioning scheme.

^c Calculated at the MP2/cc-pVDZ ground-state equilibrium geometry.

^d Calculated at the MP2/cc-pVTZ ground-state equilibrium geometry.

^e Electric dipole moment calculated at the MP2/cc-pVDZ level.

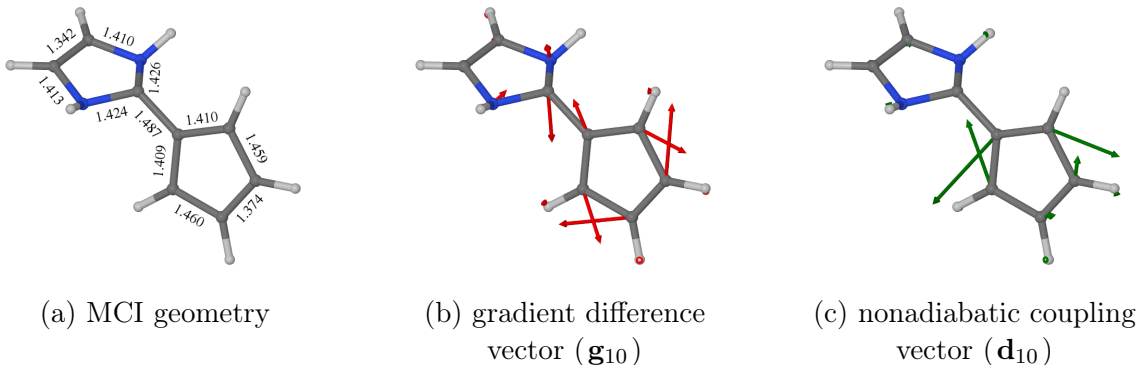
3.3 Potential Energy Surfaces

As mentioned in the previous section, the S_1 (2^1A) and S_2 (1^1B) states of compounds **II** and **III** resemble the lowest valence excited states of fulvene, though the energy ordering of the A and B symmetry states is inverted with respect to the unmodified fulvene. This similarity extends to the topography of the crossing seam between the B symmetry excited state and the electronic ground state. As has been documented by previous studies,^{69–71} the B symmetry excited state of fulvene possesses a readily accessible conical intersection (CI) seam with the ground state. This CI seam exists at all values of the twisting coordinate which describes torsion around the C5–C6 bond.^{69–71} The minimum-energy point (MCI) along this CI seam is found at a twisted geometry, where the five-membered ring and the methylene group adopt a near-perpendicular orientation.^{69–71}

An analogous CI seam between the B symmetry excited state and the ground state is found in compound **III** (and, by extrapolation, also in compound **II**). The MCI along that seam was optimized at the SA-2-CASSCF level of theory and is illustrated in Figure 6 (a). At the MCI geometry, the C_{2v} symmetry of the molecule is broken by an arching deformation of the heavy-atom skeleton, and especially the pyramidalization of atom C6. Nevertheless, inspection of the leading electronic configurations of the intersecting states shows that the S_1 adiabatic state at the MCI correlates diabatically with the 1^1B state of the molecule at its ground-state equilibrium geometry. SA-3-CASSCF calculations indicate that at the crossing seam, the S_2 adiabatic state has 2^1A diabatic character, and it is well separated in energy from the intersecting S_1 and S_0 states.

The molecular geometry at the MCI features a prominent elongation of the C1–C2, C3–C4, and C5–C6 bonds; this can be explained by noting that these three bonds have partial double-bond character in the ground state, but in the 1^1B state, the π -bonding regions of these bonds are depleted of electron density. As a consequence, the elongation of these bonds lowers the energy of the 1^1B state, while at the same time destabilizing the ground state, leading eventually to a crossing between the two. In line with this interpretation, the

Figure 6: Characterization of the S_1/S_0 MCI of compound **III** at the SA-2-CASSCF/cc-pVDZ level of theory: (a) molecular geometry at the MCI, with bond lengths marked in units of Å, (b) gradient difference vector, and (c) nonadiabatic coupling vector.



gradient difference vector between the intersecting states (see Figure 6 (b)) corresponds to the stretching of these three bonds. The nonadiabatic coupling vector (see Figure 6 (c)), in turn, mainly corresponds to another deformation of the cyclopentadienyl ring, with a contraction of the C4–C5 bond, and an elongation of the C1–C5 bond.

The PES of the 1^1B state of compound **III** is sloped in a way that drives the system from the Franck-Condon geometry (S_0 -min) towards the S_1/S_0 crossing seam. In order to demonstrate this point, we scanned the PESs along a reaction path starting at S_0 -min and ending at the S_1/S_0 MCI. The reaction path was generated by means of linear interpolation in internal coordinates (LIIC; see Ref.⁶⁴ for details). The starting point of the reaction path is the ground-state equilibrium geometry of compound **III** as optimized at the SA-2-CASSCF level of theory. The end point is the S_1/S_0 MCI, optimized at the same level of theory. Then, a set of intermediate points was generated by LIIC between these two structures. The ground- and excited-state PESs were subsequently calculated along the interpolated path with the use of the SA-3-CASSCF, XMS-CASPT2, and ADC(2) methods, all in combination with the cc-pVDZ basis set.

The results of these PES scans are illustrated in Figure 7. As noted before, at the SA-3-CASSCF level of theory the energy ordering of the 1^1B and 2^1A states at the S_0 -min

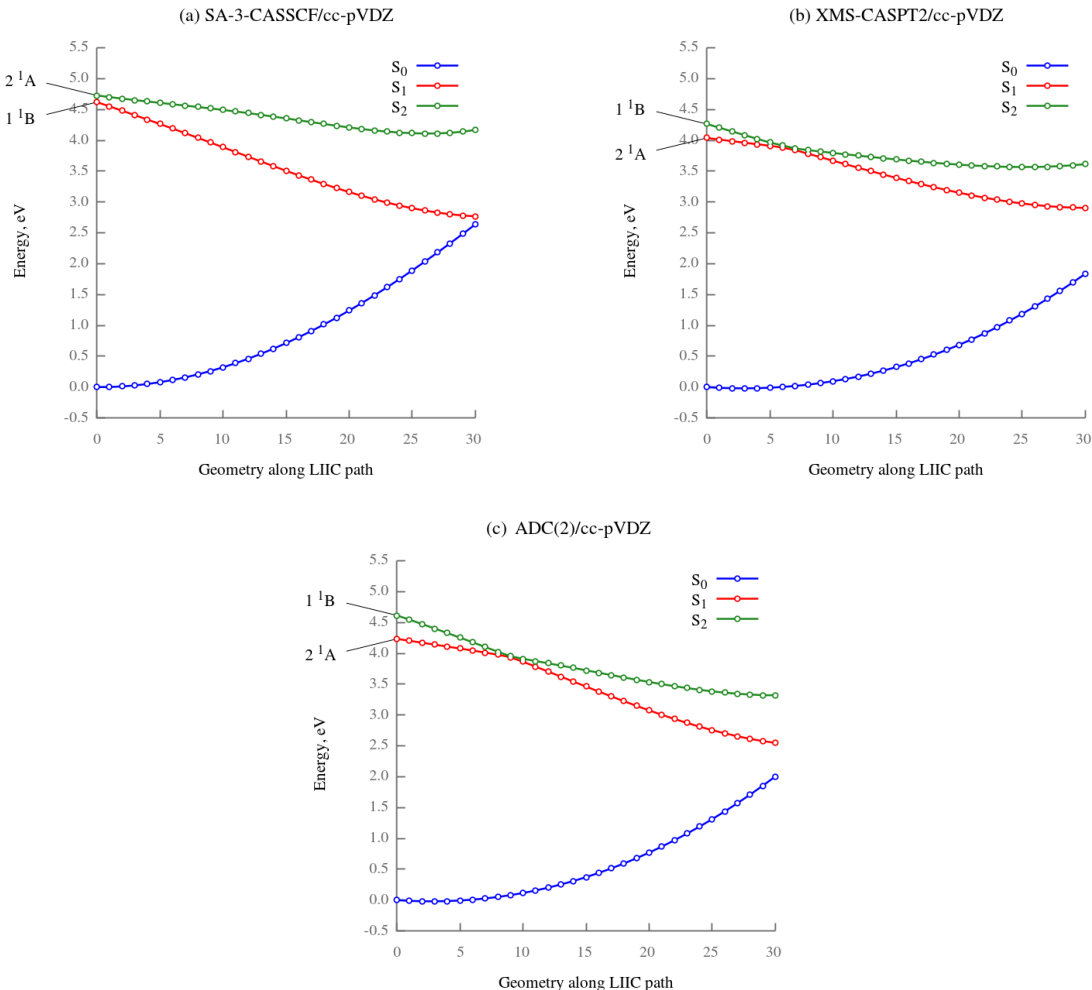
geometry is inverted with respect to the dynamically-correlated XMS-CASPT2 and ADC(2) methods. This is because the CASSCF method recovers only a small amount of dynamical correlation. As the molecule relaxes from the S_0 -min geometry towards the MCI, the energy of the 1^1B state decreases rapidly, while the energy of the ground state rises, leading ultimately to a degeneracy between the two states. Actually, at the SA-3-CASSCF level of theory, the S_1 and S_0 states at the MCI geometry are not exactly degenerate: the energy gap between them is 0.13 eV. This is due to a technical issue: the MCI had been optimized with a different stage-averaging scheme, in which only two states were included. Indeed, at the SA-2-CASSCF level, the energy gap at the MCI geometry is only 0.002 eV.

As already mentioned, at the S_0 -min geometry (optimized with SA-2-CASSCF), the XMS-CASPT2 method places the 1^1B state slightly above the 2^1A state. Furthermore, at the MCI geometry, the energy gap between the S_1 and S_0 states is fairly large, at 1.07 eV. Evidently, at the XMS-CASPT2 level of theory, the location of S_1/S_0 CI seam does not coincide with the geometry optimized at the SA-2-CASSCF level. Nevertheless, the energy gap is small enough to suggest that the CI seam does exist and lies close to the CASSCF-optimized geometry. The existence of the CI seam was additionally confirmed by a separate geometry optimization at the XMS-CASPT2 level of theory. The XMS-CASPT2-optimized MCI structure is characterized in Section S3 of the Supporting Information.

Importantly, CASSCF and XMS-CASPT2 agree in that there is no potential energy barrier on the S_1 adiabatic state along the reaction path: the energy of the S_1 state decreases monotonically on going from S_0 -min to the S_1/S_0 MCI. It follows that the CI seam is well accessible from the S_0 -min geometry, and as such it is expected to mediate internal conversion from the excited states to the ground state.

The PES scan along the LIIC path also provides an opportunity for testing the accuracy of the ADC(2) method. Although ADC(2) is not capable of providing a qualitatively correct description of CIs between electronic excited states and the ground state, in practice it is

Figure 7: PES scan of compound **III** along a path interpolated linearly from the Franck-Condon geometry (S_0 -min) to the S_1/S_0 MCI. The PESs were scanned with the use of (a) SA-3-CASSCF, (b) XMS-CASPT2, and (c) ADC(2).



often found that this method exhibits a ‘graceful failure’ behaviour. Namely, in the vicinity of a CI, the calculation remains numerically stable, and the energy gap between the MP2 ground state and the lowest ADC(2) excited state becomes small.^{52,55,64,68} Repeating the PES scan with the ADC(2) method, we find that this is also the case with the S_1/S_0 CI of compound **III**. The potential energy curves obtained with ADC(2) closely resemble those predicted by XMS-CASPT2. At the MCI optimized at the SA-2-CASSCF level, the ADC(2) calculation predicts a relatively small S_1 - S_0 energy gap of 0.54 eV. This observation indicates that ADC(2) performs well for relative energies almost up to the point where the system

reaches the CI seam.

In order to gain further insight into the topography of the S_1/S_0 CI seam, we mapped out the PESs of the S_1 and S_0 states in the space spanned by the branching space vectors – which is to say, the gradient difference vector and the derivative coupling vector. The starting point of the scan was the molecular geometry at the MCI, which we denote \mathbf{R}_{MCI} . A set of geometries in the branching space was generated with the use of the following expression:

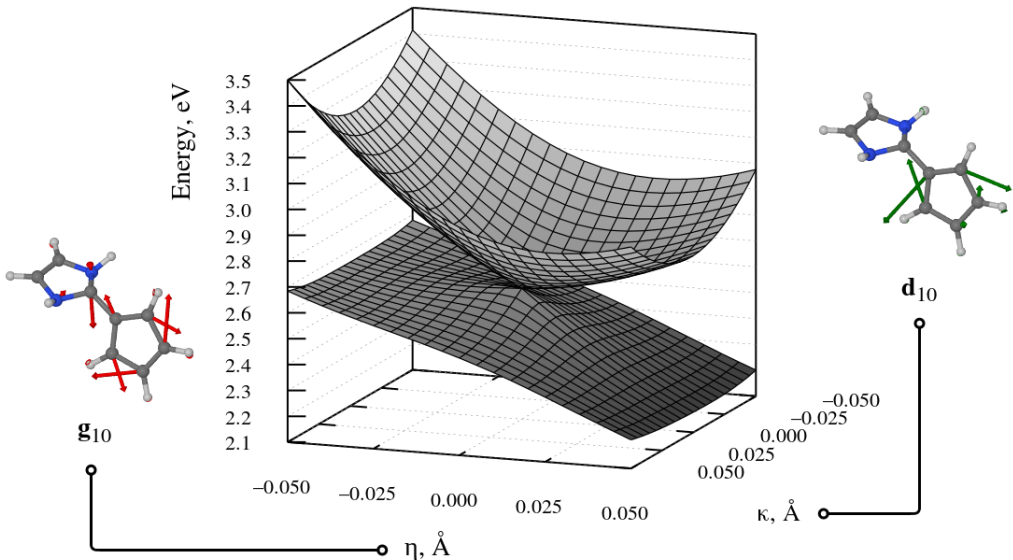
$$\mathbf{R} = \mathbf{R}_{\text{MCI}} + \kappa \frac{\mathbf{d}_{10}}{\|\mathbf{d}_{10}\|} + \eta \frac{\mathbf{g}_{10}}{\|\mathbf{g}_{10}\|} \quad (6)$$

Here, $\mathbf{d}_{10} = \langle \phi_1 | \nabla_{\mathbf{R}} | \phi_0 \rangle$ is the S_1/S_0 nonadiabatic coupling vector at the MCI, and $\mathbf{g}_{10} = \partial E_1 / \partial \mathbf{R} - \partial E_0 / \partial \mathbf{R}$ is the gradient difference vector at the MCI. (NB all of the above quantities were expressed in terms of Cartesian coordinates.) Finally, two parameters with dimension of length, κ and η , were introduced as the scan coordinates, which respectively control nuclear displacements in the direction of the nonadiabatic coupling vector, and in the direction of the gradient difference vector. These two vectors were computed at the SA-2-CASSCF level of theory at the MCI geometry optimized at the same level. Subsequently, the energies of the intersecting states were calculated at the set of geometries given by equation 6.

The results of the PES scan in the branching space coordinates are illustrated in Figure 8. It can be seen that the MCI geometry is a minimum on the S_1 state. This follows because the MCI is, by construction, a minimum along the $(3N-8)$ -dimensional CI seam. The PES scan shows that the MCI is also a minimum in the remaining two degrees of freedom available to the molecular geometry. Hence, the MCI is a true minimum on the PES of the S_1 state. Using the terminology of Ruedenberg et al.,⁷² the topography of the intersecting states can be described as peaked.

We have been unable to locate any other minimum on the PES of the S_1 state of compound **III**. Attempts to locate such a minimum result in the system relaxing towards

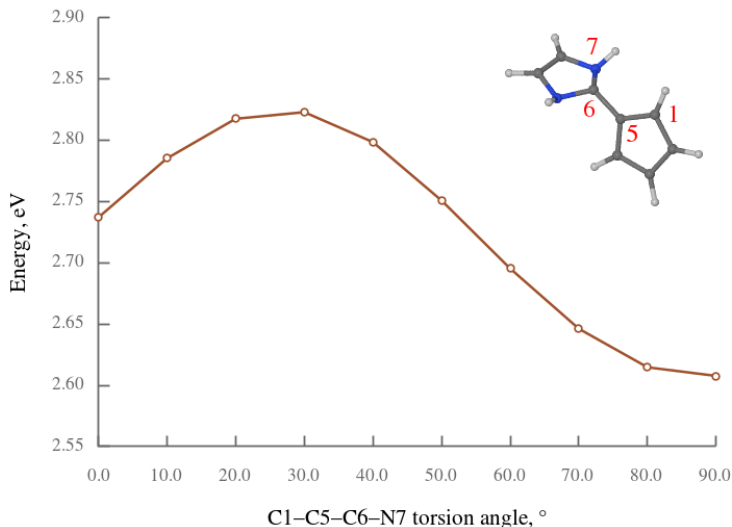
Figure 8: Topography of the S_1 and S_0 adiabatic states of compound **III** in the branching space of the S_1/S_0 MCI, as calculated at the SA-2-CASSCF level of theory. Movement along the scan coordinates κ and η corresponds to a displacement of the nuclei away from the MCI geometry along the nonadiabatic coupling vector (\mathbf{d}_{10}) and the gradient difference vector (\mathbf{g}_{10}), respectively. The two branching space vectors are shown in insets on either side of the graph; see also Figure 6 and the accompanying text. The MCI itself is located at $\kappa = \eta = 0$. The zero of the energy scale corresponds to the energy of the S_0 -min structure as optimized with SA-2-CASSCF.



the S_1/S_0 CI seam. Most likely, the MCI geometry represents the only minimum on the S_1 state. As a consequence, the S_2 and S_1 states are not expected to be able to trap the excited-state population for an extended period of time.

It can also be shown that the S_1/S_0 CI seam of compound **III** exists over a wide range of twisting angles. To this end, we scanned the energies of the intersecting states as a function of the C1–C5–C6–N7 torsion angle. More specifically, the minimum along the CI seam was reoptimized at each scan point, subject to the constraint that the C1–C5–C6–N7 torsion angle be fixed. The C1–C5–C6–N7 torsion angle was varied from 0° to 90° in increments of 10° . As before, the optimizations were performed at the SA-2-CASSCF level of theory. The results of the scan are shown in Figure 9. The CI seam can be seen to extend over the entire range of torsion angles taken into consideration, with only relatively little variation in

Figure 9: PES scan along the S_1/S_0 CI seam of compound **III**. In this scan, the C1–C5–C6–N7 torsion angle was constrained while other internal coordinates were reoptimized at each scan point (a so-called relaxed PES scan). The zero of the energy scale corresponds to the energy of the S_0 -min structure as optimized with SA-2-CASSCF. For ease of reference, the inset at the top right shows the atom numbering.



energy.

In Figure 10, the results of the PES scans have been combined to form a qualitative picture of the overall photophysics of compound **II**. The branching space coordinates collectively represent bond length changes and the pyramidalization of atom C6, both of which play an important role in controlling the relative energies of the relevant electronic states. The twisting coordinate corresponds to torsion around the central C5–C6 bond. As mentioned in Section 3.1, the ground-state equilibrium geometry of compound **II** exhibits a slight twist around the central C5–C6 bond (see Figure 3 (a)). For this reason, two symmetry-equivalent minima appear on the PES of the 1^1A state, of which one corresponds to a clockwise-twisted geometry, and the other to a counterclockwise-twisted geometry.

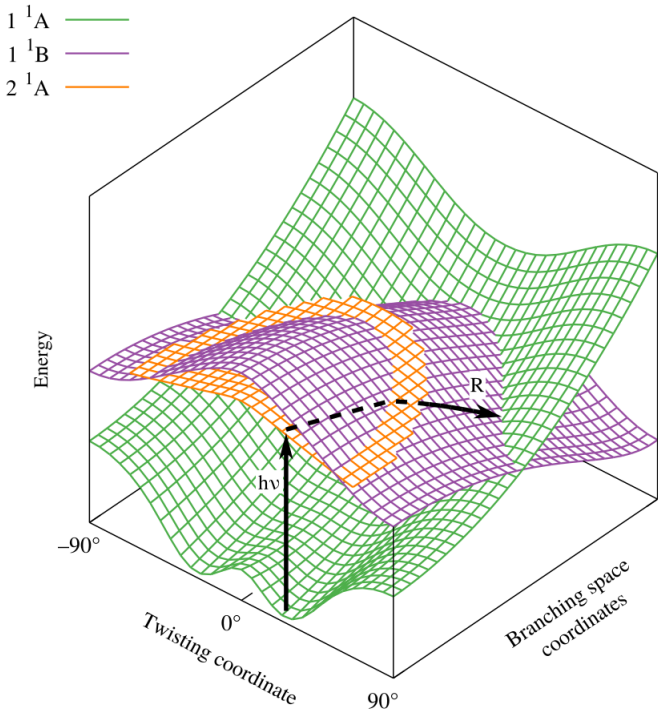
The irradiation of the lowest photoabsorption band populates the bright 2^1A state, initiating the relaxation process. In Figure 10, this initial photoexcitation event is indicated with a vertical black arrow labeled ' $h\nu$ '. Subsequently, some fraction of the excited-state population will undergo a radiationless transition into the dark 1^1B state. The population

transfer from the 2^1A state into the 1^1B state will be facilitated by the small energy gap between these states in the Frank-Condon region of the molecule.

Once the system is in the 1^1B state, the steep slope of the PES of that state drives the system towards the CI seam with the 1^1A state. In Figure 10, the movement towards the CI seam is indicated with the curving arrow labeled ‘R.’ At the CI seam, the excited-state population returns into the 1^1A state. This internal conversion process will be followed by vibrational cooling and a relaxation back towards the ground-state geometry.

Anticipating the results of the nonadiabatic molecular dynamics simulations, which are presented in the next section, we expect that while the molecule remains in the excited electronic states, the nuclear wavepacket will spread out somewhat along the twisting coordinate, and will reach the S_1/S_0 CI seam at geometries ranging from slightly-twisted to near-perpendicular. In a population of many molecules, some will undergoes a full rotation around the central C5–C6 bond. At the same time, however, our calculations indicate that compound **II** is not suited to the role of a molecular switch or a molecular motor. This is because the CI seam is also accessible at non-twisted geometries. One can imagine a hypothetical situation where the rotation around the C5–C6 bond is partially arrested by an external force acting on the cyclopentadienyl and tetramethylimidazolium moieties. In this case, the system can still reach the segment of the S_1/S_0 CI seam which exists at near-planar, or slightly twisted geometries. In this manner, the molecule will undergo radiationless deactivation without a twist around the C5–C6 bond.

Figure 10: Schematic illustration of the ground- and excited-state PESs of compound **II**. Part of the surface which represents the 2^1A state is cut off so as to reveal the surfaces of the 1^1A and 1^1B states, which lie partially underneath. The arrow labeled ' $h\nu$ ' represents vertical excitation into the spectroscopically bright S_1 (2^1A) state. The arrow labeled ' R ' indicates the relaxation of the system from the Franck-Condon geometry to the crossing seam between the 1^1B and 1^1A states. The dashed part of this arrow represents movement on the potential energy surface of the 2^1A state, which initially lies beneath the surface of the 1^1B state.



3.4 Nonadiabatic Molecular Dynamics

Having examined the ground- and excited-state PESs of compound **II**, we are now prepared to discuss the relaxation process resulting from the irradiation of its lowest photoabsorption band. The classical populations of the adiabatic states included in the FSSH simulations are plotted in Figure 11 (a). Panel (b) of the same Figure shows the time-evolution of parameter $\bar{\mu}_{0n}$, which provides information on the diabatic character of the currently occupied state along the simulated trajectories. Panels (c) and (d), in turn, characterize the time-evolution of molecular geometry: the angle α , which is the angle formed by the central C5–C6 bond

and the plane defined by atoms C6, N7, and N10, and parameter τ , which describes torsion around the C5–C6 bond.

The majority of simulated trajectories (32 out of 40, or 80% of the total number) began in the S_1 state, and the remainder were initially occupying the S_2 state. The reason that as many as 8 simulated trajectories (20% of the total number) began in the S_2 state is because the starting geometries had been sampled from the Wigner distribution, and were subject to vibrational displacements from the ground-state equilibrium geometry. These small displacements broke the C_2 symmetry of the ground-state equilibrium geometry. At some of the displaced geometries, there was mixing between the S_1 (2^1A) and S_2 (1^1B) states, such that the S_2 (1^1B) state acquired an admixture of 2^1A character, and vice versa. At such geometries, the $S_0 \rightarrow S_2$ transition had appreciable oscillator strength, which increased the likelihood of the S_2 state being populated. This mixing effect can be seen in Figure 5 (b) in Section 3.2, where the simulated photoabsorption spectrum is broken down into contributions from transitions into the individual adiabatic excited states. Due to mixing between the S_1 and S_2 states, the S_2 state makes a significant contribution to the total photoabsorption in the energy range from around 3.6 eV to around 4.4 eV.

At the outset of the simulated relaxation dynamics, the bending angle α in the ensemble of simulated trajectories was distributed in the range of around 170° to around 190° . The twisting angle τ , in turn, was distributed in the range of around 25° to around 45° . (The spread in parameters α and τ reflects the spatial distribution of the nuclear wavefunction of the molecule in its electronic ground state.)

At $t = 0$, immediately after the initial photoexcitation, the parameter $\bar{\mu}_{0n}$ took a value of 2.18 a.u.. This comes very close in magnitude to the transition dipole moment of the $S_0 \rightarrow S_1$ (2^1A) transition at the ground-state equilibrium geometry, which is 2.38 a.u.. This observation confirms that at the outset of the relaxation process, the diabatic character of the occupied state was predominantly 2^1A .

During the initial 20 fs-long period of the simulated dynamics, most of the trajectories

which began in the S_2 adiabatic state underwent a hop to the S_1 state. After $t = 20$ fs following the initial photoexcitation, the classical population of the S_2 state fluctuated near a value of 0.05 before dropping to zero at around $t = 110$ fs. The initial 20 fs period of the relaxation process was also marked by a steady decrease in the value of parameter $\bar{\mu}_{0n}$, which we attribute to a combination of two phenomena. Firstly, the diabatic character of the currently occupied state among the simulated trajectories shifts from predominantly 2^1A towards intermediate between 2^1A and 1^1B . Secondly, at this stage of the relaxation process, the molecular skeleton begins to undergo an arching deformation, which, presumably, reduces the overlap between the occupied and virtual orbitals involved in the transitions from the ground state to both of the lowest two singlet excited states.

The arching deformation mentioned above involved the pyramidalization of carbon atom C6, and its progress can be followed by examining the bending angle α . At $t = 0$, the nuclear wavepacket was localized in a small region of configuration space around the ground-state equilibrium geometry, and values of α from the individual trajectories were distributed narrowly around a value of 180° . Over the next few tens of femtoseconds, the individual trajectories diverged away from $\alpha = 180^\circ$ while atom C6 became pyramidalized. Also, during the initial stage of the relaxation process, the cyclopentadienyl moiety began to rotate relative to the tetramethylimidazolium moiety around the axis formed by the central C5–C6 bond.

The onset of internal conversion to the ground state occurred already 25 fs after the initial photoexcitation. In a short space of time from $t = 25$ fs until $t = 40$ fs, 10 from among the simulated trajectories (25% of the total number) approached the S_1/S_0 CI seam to within 0.25 eV, and were considered to be undergoing internal conversion to the ground state. In all of these trajectories, at the time that the molecule approached the CI seam, carbon atom C6 was substantially pyramidalized, but the molecule had not had time to undergo a significant rotation around the C5–C6 bond.

In the surviving trajectories, atom C6 remained pyramidalized for the remainder of the

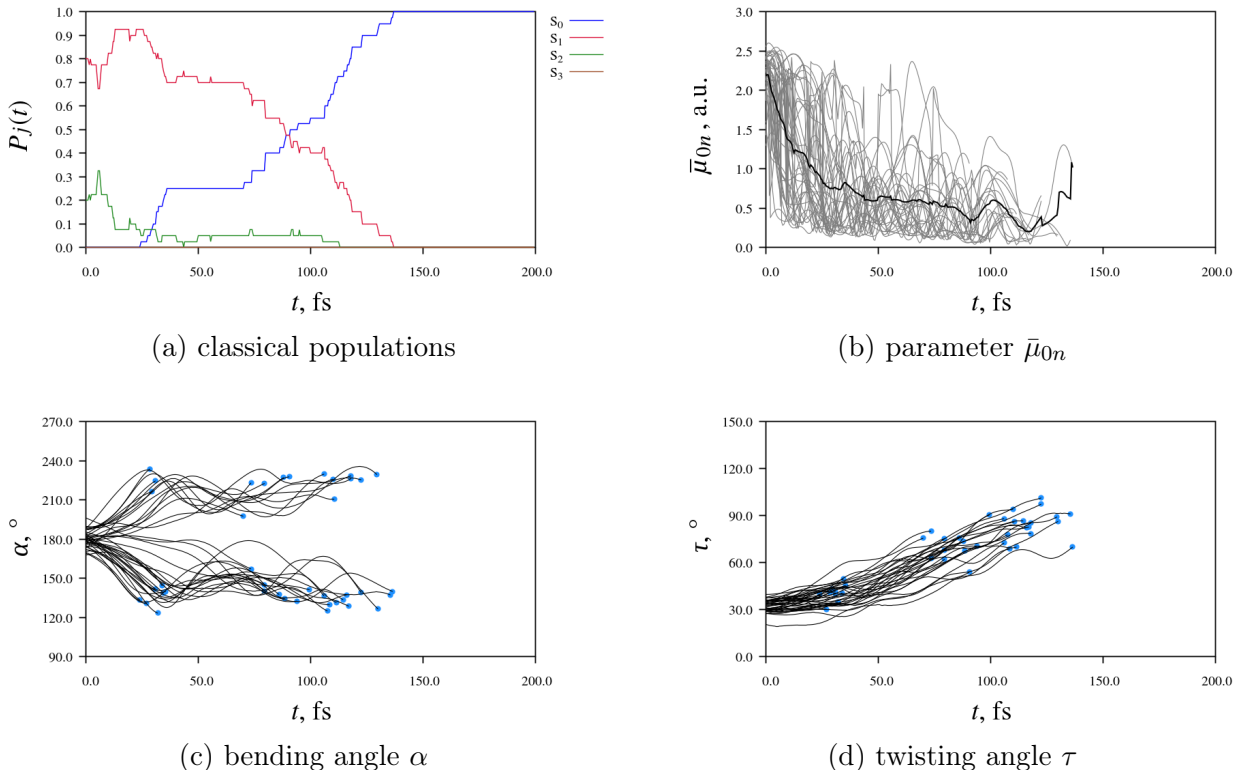
simulation time. Meanwhile, the cyclopentadienyl moiety continued its rotation around the C5–C6 bond. These trajectories began reaching the S_1/S_0 crossing seam at $t = 70$ fs, at trajectories ranging from partially twisted ($\tau \approx 60^\circ$) to fully twisted ($\tau \approx 90^\circ$). All of the simulated trajectories had encountered the crossing seam by $t = 140$ fs. The median time of internal conversion from among the entire ensemble of simulated trajectories was 92 fs.

Accompanying this narrative, as part of the Supporting Information we provide animations of three representative simulated trajectories. Each animation shows the time-evolution of the molecular geometry, and the energies and populations of the S_0 , S_1 , and S_2 states. The passage of time is indicated with a vertical black line moving along the time axis. The currently occupied state is marked with a black circle.

The relaxation mechanism of compound **II** is partially similar to that of fulvene excited initially into the S_1 (1^1B_2) state. Both compound **II** and fulvene undergo internal conversion to the singlet ground state at the extended CI seam between the B-symmetry excited state and the ground state. One important difference is that in fulvene, the internal conversion process takes place at a narrow segment of the S_1/S_0 crossing seam at near-planar geometries. In the case of compound **II**, however, reaching the CI seam requires the pyramidalization of atom C6. During the relaxation process of compound **II**, the nuclear wavepacket spreads out somewhat, and reaches a fairly broad segment of the S_1/S_0 crossing seam extending from slightly twisted to fully twisted geometries. Still, torsion around the C5–C6 bond is clearly not a prerequisite for reaching the CI seam.

In order to gain insight into possible solvent effects in the photophysics of compound **II**, we additionally performed another set of simulations in which a molecule of this compound was placed at the center of a water droplet. A detailed summary of these calculations is given in Section S4 of the Supporting Information. In the event, it turns out that the relaxation process of compound **II** is only slightly affected by polar solvation. In water, it undergoes internal conversion to the ground state via the same mechanism as in the isolated-molecule simulations. Although in solution phase, the excited-state lifetime is longer by a factor of

Figure 11: Time-evolution of electronic structure and molecular geometry during the relaxation dynamics of compound **II**. Parameter $\bar{\mu}_{0n}$ quantifies the transition dipole moment of the occupied state in the ensemble of trajectories; see Section 2.2 for details. α is the angle formed by the C5–C6 bond, and the plane defined by atoms C6, N7 and N10. τ is the average of the dihedral angles C1–C5–C6–N7 and C4–C5–C6–N10. In panels (c) and (d), the point in time at which a given trajectory was discontinued is indicated with a blue dot.



around 2 than under isolated-molecule conditions, it is still relatively short. In summary, compound **II** appears fairly insensitive to polar solvation.

4 Conclusions

In this contribution, we have investigated the electronic structure and photophysics of compound **II**, a donor-acceptor system comprising a cyclopentadienyl moiety and a tetramethylimidazolium moiety. In the singlet ground state, compound **II** is strongly polar and, what is more, both of its constituent five-membered rings can be described as having partial aromatic character.

Despite the highly polar nature of the ground electronic state, the photophysics of compound **II** largely parallels the case of the unsubstituted fulvene. The similarities begin with the structures of the lowest two valence excited states. While these states feature a substantial redistribution of electron density from the cyclopentadienyl moiety onto the tetramethylimidazole moiety, they also retain some similarity to the lowest two singlet valence excited states of fulvene. In the case of the 1^1B state, the resemblance extends to the topography of the conical intersection seam with the ground state. This conical intersection seam lies roughly parallel to the intramolecular twisting coordinate which describes the relative orientation of the cyclopentadienyl and tetramethylimidazolium moieties. Although the lowest point along the seam is found at a geometry where the two five-membered rings are twisted relative to one another, the intramolecular rotation is not a prerequisite for reaching the seam. Figuratively speaking, compound **II** twists only opportunistically, when rotation around the central C5–C6 is not hindered by external factors.

Following initial excitation into the bright 2^1A state, compound **II** undergoes internal conversion into the 1^1B state, which in turn returns to the electronic ground state at the abovementioned crossing seam. The ground electronic state is fully repopulated within around 150 fs of photoexcitation.

Given that the incorporation of the exocyclic carbon atom (C6) of fulvene into the strongly electron-donating imidazole-like moiety has relatively little effect on the topography of the S_1/S_0 crossing seam, it does not appear to represent a viable strategy for the design of a molecular switch based on E/Z -photoisomerization around a double bond. It is nevertheless quite remarkable that the relaxation process of compound **II** proceeds through a $\pi\pi^*$ state with clear-cut ICT character. In typical aromatic donor-acceptor systems of comparable size, such as *N*-phenylpyrrole and its derivatives, ICT states are populated only in sufficiently polar environments.^{73–75} Thus, the design strategy embodied in compound **II** may well lead to photoactive molecules possessing low-lying ICT states.

■ Associated Content

Supporting Information

Ground-state electronic structure of compound **II**, Rydberg-type excited states of compound **II**, optimization of the MCI of compound **III** at the XMS-CASPT2 level of theory, photophysics of compound **II** in polar solution (PDF). Animations of representative simulated trajectories (MP4). LIIC path leading from the Franck-Condon geometry of compound **III** to the S_1/S_0 MCI (ZIP).

■ Author Information

Corresponding Author

*E-mail: michal.kochman@liu.se

Phone: +46-(0)701-697-673

*E-mail: bodur@ifm.liu.se

Phone: +46-(0)13-28 24 97

ORCID

Michał A. Kochman: 0000-0003-2552-9464

Bo Durbeej: 0000-0001-5847-1196

Notes

The authors declare no competing financial interest.

■ Acknowledgements

The authors are indebted to Dr Johan Raber for invaluable technical assistance. We gratefully acknowledge financial support from Stiftelsen Olle Engkvist Byggmästare (grant 184-568), from Wenner-Gren Stiftelserna (grant UPD2018-0102), and from Linköping University. We would also like to thank the National Supercomputer Center (NSC) in Linköping, Sweden, for their generous allotment of computer time.

■ References

- (1) Hartke, K.; Salamon, G. Im 5-Ring Unsubstituierte 6.6-Diamino-fulvene. *Chem. Ber.* **1970**, *103*, 133-146. DOI: 10.1002/cber.19701030120
- (2) Hartke, K.; Salamon, G. Im 5-Ring Negativ Substituierte 6.6-Diamino-fulvene. *Chem. Ber.* **1970**, *103*, 147-155. DOI: 10.1002/cber.19701030121
- (3) Wu, Y.-L.; Bureš, F.; Jarowski, P. D.; Schweizer, W. B.; Boudon, C.; Gisselbrecht, J.-P.; Diederich, F. Proaromaticity: Organic Charge-Transfer Chromophores with Small HOMO-LUMO Gaps. *Chem. Eur. J.* **2010**, *16*, 9592-9605. DOI: 10.1002/chem.201001051
- (4) Jarjis, H. M.; Khalil, S. M. A Theoretical Study of Monosubstituted Fulvenes. *Z. Naturforsch. A* **1990**, *45*, 799-806. DOI: 10.1515/zna-1990-0607
- (5) Krygowski, T. M.; Ciesielski, A.; Cyrański, M. Aromatic Character and Energy of the Five- and Seven-Membered Rings in Derivatives of Penta- and Heptafulvene Substituted in Exocyclic Position. *Chem. Papers* **1995**, *49*, 128-132. <https://www.chempap.org/?id=7&paper=3562>
- (6) Stepień, B. T.; Krygowski, T. M.; Cyrański, M. K. Extent of Cyclic π -Electron

- Delocalization Modification in Exocyclically Substituted Fulvenes. *J. Org. Chem.* **2002**, *67*, 5987-5992. DOI: 10.1021/jo025762m
- (7) Krygowski, T. M.; Oziminski, W. P.; Palusiak, M.; Fowler, P. W.; McKenzie, A. D. Aromaticity of Substituted Fulvene Derivatives: Substituent-Dependent Ring Currents. *Phys. Chem. Chem. Phys.* **2010**, *12*, 10740-10745. DOI: 10.1039/c003686b
- (8) Oziminski, W. P.; Krygowski, T. M. Natural Bond Orbital Approach to the Transmission of Substituent Effect through the Fulvene and Benzene Ring Systems. *J. Mol. Model.* **2011**, *17*, 565-572. DOI 10.1007/s00894-010-0753-1
- (9) Oziminski, W. P.; Krygowski, T. M. Aromatization of Rings of Fulvene and Heptafulvene due to the Through Space Interactions in [3₄]3,4,6,6-fulvene-4,5,8,8-heptafulvene-cyclophane. *Comput. Theor. Chem.* **2011**, *965*, 240-243. DOI: 10.1016/j.comptc.2011.02.010
- (10) Neuenschwander, M. Substituent Effects on π -Bond Delocalization of Fulvenes and Fulvalenes. Are Fulvenes Aromatic? *Helv. Chim. Acta* **2015**, *98*, 763-784. DOI: 10.1002/hlca.201400211
- (11) Sadlej-Sosnowska, N. Electronic Properties and Aromaticity of Substituted Diphenylfulvenes in the Ground (S_0) and Excited (T_1) States. *Struct. Chem.* **2018**, *29*, 23-31. DOI: 10.1007/s11224-017-0995-y
- (12) Aqad, E.; Leriche, P.; Mabon, G.; Gorgues, A.; Khodorkovsky, V. Novel D- π -A Chromophores Based on the Fulvene Accepting Moiety. *Org. Lett.* **2001**, *3*, 2329-2332. DOI: 10.1021/ol016143n
- (13) Shurdha, E.; Repasy, B. K.; Miller, H. A.; Dees, K.; Iacono, S. T.; Ball, D. W.; Balaich, G. J. Symmetrical Bis(Fulvene) Chromophores: Model Compounds for *Acceptor-Donor-Acceptor* Dye Architectures. *RSC Adv.* **2014**, *4*, 41989-41992. DOI: 10.1039/c4ra07738e

- (14) Kerisit, N.; Finke, A. D.; Trapp, N.; Leroux, Y. R.; Guillemin, J.-C.; Trolez, Y.; Diederich, F. New Reactivity of 6,6-Bis-Donor-Substituted Pentafulvenes: One-Step Synthesis of Highly Substituted [3]Cumulene and Dihydropentalene. *Tetrahedron* **2015**, *71*, 4393-4399. DOI: 10.1016/j.tet.2015.03.081
- (15) Kawase, T.; Kurata, H. (2016). Recent Developments in Fulvene and Heterofulvene Chemistry. In *Cross Conjugation: Modern Dendralene, Radialene and Fulvene Chemistry*; Hopf, H.; Sherburn, M. S., Eds.; Wiley-VCH: Weinheim, Germany, 2016; pp 145-236. doi:10.1002/9783527671182.ch6
- (16) Preethalayam, P.; Krishnan, K. S.; Thulasi, S.; Chand, S. S.; Joseph, J.; Nair, V.; Jaroschik, F.; Radhakrishnan, K. V. Recent Advances in the Chemistry of Pentafulvenes. *Chem. Rev.* **2017**, *117*, 3930-3989. DOI: 10.1021/acs.chemrev.6b00210
- (17) Haberland, S.; Finke, A. D.; Kerisit, N.; Katan, C.; Trolez, Y.; Gawel, P.; Leito, I.; Lõkov, M.; Järviste, R.; Kaupmees, K.; Trapp, N.; Ruhlmann, L.; Boudon, C.; Himmel, D.; Diederich, F. Enhancement of Push-Pull Properties of Pentafulvene and Pentafulvalene Derivatives by Protonation at Carbon. *Eur. J. Org. Chem.* **2018**, 739-749. DOI: 10.1002/ejoc.201800039
- (18) Haas, Y.; Cogan, S.; Zilberg, S. The Use of Elementary Reaction Coordinates in the Search for Conical Intersections. *Int. J. Quantum Chem.* **2005**, *102*, 961-970. DOI: 10.1002/qua.20460
- (19) Cogan, S.; Kahan, A.; Zilberg, S.; Haas, Y. Photophysics of (1-Butyl-4-(1H-inden-1-ylidene)-1,4-dihydropyridine (BIDP): An Experimental Test for Conical Intersections. *J. Phys. Chem. A* **2008**, *112*, 5604-5612. DOI: 10.1021/jp7110296
- (20) Alfalah, S.; Deeb, O.; Zilberg, S.; Haas, Y. Solvent Effect on the Conical Intersection

- of 4-Cyclopentadienylidene-1,4-dihydropyridine (CPDHP). *Chem. Phys. Lett.* **2008**, *459*, 100-104. DOI: 10.1016/j.cplett.2008.05.024
- (21) Berson, J. A.; Evleth, E. M.; Hamlet, Z. Nitrogen Analogs of Sesquifulvalene. I. Synthesis and Properties. *J. Am. Chem. Soc.* **1965**, *87*, 2887-2900. DOI: 10.1021/ja01091a019
- (22) Berson, J. A.; Evleth, E. M., Jr.; Manatt, S. L. Nitrogen Analogs of Sesquifulvalene. II. Theoretical Correlation of Ground-State Properties. *J. Am. Chem. Soc.* **1965**, *87*, 2901-2908. DOI: 10.1021/ja01091a020
- (23) Evleth, E. M., Jr.; Berson, J. A.; Manatt, S. L. Nitrogen Analogs of Sesquifulvalene. III. Theoretical Correlation of Excited-State Properties. *J. Am. Chem. Soc.* **1965**, *87*, 2908-2913. DOI: 10.1021/ja01091a021
- (24) Oruganti, B.; Wang, J.; Durbeej, B. Excited-State Aromaticity Improves Molecular Motors: A Computational Analysis. *Org. Lett.* **2017**, *19*, 4818-4821. DOI: 10.1021/acs.orglett.7b02257
- (25) Durbeej, B.; Wang, J.; Oruganti, B. Molecular Photoswitching Aided by Excited-State Aromaticity. *ChemPlusChem* **2018**, *83*, 958-967. DOI: 10.1002/cplu.201800307
- (26) Kunz, D.; Johnsen, E. Ø.; Monsler, B.; Rominger, F. Highly Ylidic Imidazoline-Based Fulvenes as Suitable Precursors for the Synthesis of Imidazolium-Substituted Metallocenes. *Chem. Eur. J.* **2008**, *14*, 10909-10914. DOI: 10.1002/chem.200801956
- (27) Schmid, D.; Seyboldt, A.; Kunz, D. A Direct Synthesis of a Strongly Zwitterionic 6,6'-Diaminofulvalene. *Z. Naturforsch.* **2014**, *69b*, 580-588. DOI: 10.5560/ZNB.2014-4015

- (28) Schmid, D.; Seyboldt, A.; Kunz, D. Reaction of Iron- and Tungsten Carbonyls with a Zwitterionic Fulvalene. *Z. Anorg. Allg. Chem.* **2015**, *641*, 2228-2232. DOI: 10.1002/zaac.201500564
- (29) Schmid, D.; Seyboldt, A.; Eichele, K.; Kunz, D. Synthesis of a Lithium-Cyclopentadienide Complex by Addition of LiNTf₂ to a Zwitterionic Fulvalene. *Dalton Trans.* **2017**, *46*, 29-32. DOI: 10.1039/c6dt03355e
- (30) Roos, B. O. The Complete Active Space Self-Consistent Field Method and its Applications in Electronic Structure Calculations. *Adv. Chem. Phys.* **1987**, *69*, 399-445. DOI: 10.1002/9780470142943.ch7
- (31) Shiozaki, T.; Győrffy, W.; Celani, P.; Werner, H.-J. Communication: Extended Multi-State Complete Active Space Second-Order Perturbation Theory: Energy and Nuclear Gradients. *J. Chem. Phys.* **2011**, *135*, 081106. DOI: 10.1063/1.3633329
- (32) BAGEL, Brilliantly Advanced General Electronic-structure Library. <http://www.nubakery.org> under the GNU General Public License.
- (33) Shiozaki, T. BAGEL: Brilliantly Advanced General Electronic-structure Library. *WIREs Comput. Mol. Sci.* **2017**, e1331. DOI: 10.1002/wcms.1331
- (34) Dunning Jr, T. H. Gaussian Basis Sets for Use in Correlated Molecular Calculations. I. The Atoms Boron Through Neon and Hydrogen. *J. Chem. Phys.* **1989**, *90*, 1007-1023. DOI: 10.1063/1.456153
- (35) Finley, J.; Malmqvist, P.-A.; Roos, B. O.; Serrano-Andrés, L. The Multi-State CASPT2 Method. *Chem. Phys. Lett.* **1998**, *288*, 299-306. DOI: 10.1016/S0009-2614(98)00252-8
- (36) Trofimov, A. B.; Schirmer, J. An Efficient Polarization Propagator Approach to

- Valence Electron Excitation Spectra. *J. Phys. B: At., Mol. Opt. Phys.* **1995**, *28*, 2299-2324, DOI: 10.1088/0953-4075/28/12/003.
- (37) Hättig, C. Structure Optimizations for Excited States with Correlated Second-Order Methods: CC2 and ADC(2). In *Advances in Quantum Chemistry*; Jensen, H. J. Å., Ed.; Academic Press: New York, 2005; Vol. 50; pp 37-60. DOI: 10.1016/S0065-3276(05)50003-0.
- (38) TURBOMOLE V6.3.1 2011, a development of University of Karlsruhe and Forschungszentrum Karlsruhe GmbH, 1989-2007, TURBOMOLE GmbH, since 2007; available from <http://www.turbomole.com>.
- (39) Haase, F.; Ahlrichs, R. Semi-direct MP2 Gradient Evaluation on Workstation Computers: The MPGRAD Program. *J. Comp. Chem.*, **1993**, *14*, 907-912, DOI: 10.1002/jcc.540140805
- (40) Weigend, F.; Häser, M. RI-MP2: First Derivatives and Global Consistency. *Theor. Chem. Acc.*, **1997**, *97*, 331-340, DOI: 10.1007/s002140050269
- (41) Hättig, C.; Weigend, F. CC2 Excitation Energy Calculations on Large Molecules Using the Resolution of the Identity Approximation. *J. Chem. Phys.*, **2000**, *113*, 5154-5161, DOI: 10.1063/1.1290013
- (42) Köhn, A.; Hättig, C. Analytic Gradients for Excited States in the Coupled-Cluster Model CC2 Employing the Resolution-of-the-Identity Approximation. *J. Chem. Phys.*, **2003**, *119*, 5021-5036, DOI: 10.1063/1.1597635
- (43) Weigend, F.; Köhn, A.; Hättig, C. Efficient Use of the Correlation Consistent Basis Sets in Resolution of the Identity MP2 Calculations. *J. Chem. Phys.*, **2002**, *116*, 3175-3183, DOI: 10.1063/1.1445115

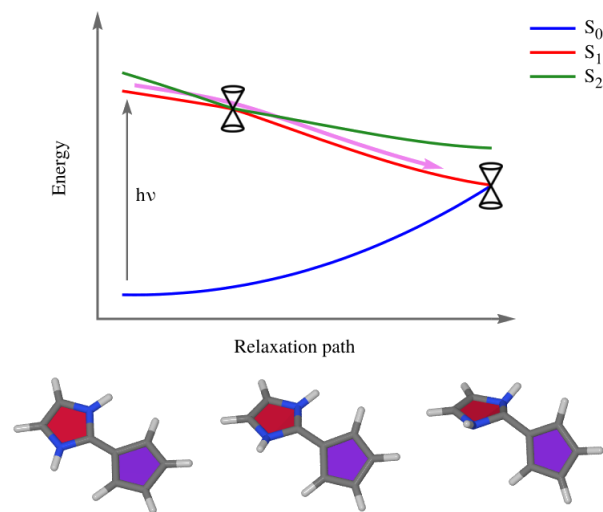
- (44) Robin, M. R. *Highly Excited States of Polyatomic Molecules* Academic Press: New York and London, 1974.
- (45) Besley, N. A.; Hirst, J. D. Ab Initio Study of the Electronic Spectrum of Formamide with Explicit Solvent. *J. Am. Chem. Soc.* **1999**, *121*, 8559-8566. DOI: 10.1021/ja990064d
- (46) Szalay, P. G.; Watson, T.; Perera, A.; Lotrich, V.; Fogarasi, G.; Bartlett, R. J. Benchmark Studies on the Building Blocks of DNA. 2. Effect of Biological Environment on the Electronic Excitation Spectrum of Nucleobases. *J. Phys. Chem. A* **2012**, *116*, 8851-8860. DOI: 10.1021/jp305130q
- (47) Tully, J. C.; Preston, R. K. Trajectory Surface Hopping Approach to Nonadiabatic Molecular Collisions: The Reaction of H^+ with D_2 . *J. Chem. Phys.* **1971**, *55*, 562-572. DOI: 10.1063/1.1675788
- (48) Tully, J. C. Molecular Dynamics with Electronic Transitions. *J. Chem. Phys.* **1990**, *93*, 1061-1071. DOI: 10.1063/1.459170
- (49) Hammes-Schiffer, S.; Tully, J. C. Proton Transfer in Solution: Molecular Dynamics With Quantum Transitions. *J. Chem. Phys.* **1994**, *101*, 4657-4667. DOI: 10.1063/1.467455
- (50) Doltsinis, N. L.; Marx, D. First Principles Molecular Dynamics Involving Excited States and Nonadiabatic Transitions. *J. Theor. Comput. Chem.* **2002**, *1*, 319-349. DOI: 10.1142/S0219633602000257
- (51) Barbatti, M.; Granucci, G.; Ruckebauer, M.; Plasser, F.; Crespo-Otero, R.; Pittner, J.; Persico, M.; Lischka, H. NEWTON-X: a package for Newtonian dynamics close to the crossing seam, version 2.0, www.newtonx.org (2017).

- (52) Plasser, F.; Crespo-Otero, R.; Pederzoli, M.; Pittner, J.; Lischka, H.; Barbatti, M. Surface Hopping Dynamics with Correlated Single-Reference Methods: 9H-Adenine as a Case Study. *J. Chem. Theory Comput.* **2014**, *10*, 1395-1405. DOI: 10.1021/ct4011079
- (53) Barbatti, M.; Granucci, G.; Persico, M.; Ruckenbauer, M.; Vazdar, M.; Eckert-Maksic, M.; Lischka, H. The On-the-Fly Surface-Hopping Program System Newton-X: Application to *Ab Initio* Simulation of the Nonadiabatic Photodynamics of Benchmark Systems. *J. Photochem. Photobiol., A* **2007**, *190*, 228-240. DOI: 10.1016/j.jphotochem.2006.12.008
- (54) Barbatti, M.; Ruckenbauer, M.; Plasser, F.; Pittner, J.; Granucci, G.; Persico, M.; Lischka, H. Newton-X: a Surface-Hopping Program for Nonadiabatic Molecular Dynamics. *Wiley Interdiscip. Rev.: Comput. Mol. Sci.* **2014**, *4*, 26-33. DOI: 10.1002/wcms.1158
- (55) Tuna, D.; Lefrancois, D.; Wolański, Ł.; Gozem, S.; Schapiro, I.; Andruniów, T.; Dreuw, A.; Olivucci, M. Assessment of Approximate Coupled-Cluster and Algebraic-Diagrammatic-Construction Methods for Ground- and Excited-State Reaction Paths and the Conical-Intersection Seam of a Retinal-Chromophore Model. *J. Chem. Theory Comput.* **2015**, *11*, 5758-5781. DOI: 10.1021/acs.jctc.5b00022
- (56) Lefrancois, D.; Tuna, D.; Martínez, T. J.; Dreuw, A. The Spin-Flip Variant of the Algebraic-Diagrammatic Construction Yields the Correct Topology of S_1/S_0 Conical Intersections. *J. Chem. Theory Comput.* **2017**, *13*, 4436-4441. DOI: 10.1021/acs.jctc.7b00634
- (57) Ryabinkin, I. G.; Nagesh, J.; Izmaylov, A. F. Fast Numerical Evaluation of Time-Derivative Nonadiabatic Couplings for Mixed Quantum-Classical Methods. *J. Phys. Chem. Lett.* **2015**, *6*, 4200-4203. DOI: 10.1021/acs.jpcllett.5b02062

- (58) Granucci, G.; Persico, M. Critical Appraisal of the Fewest Switches Algorithm for Surface Hopping. *J. Chem. Phys.* **2007**, *126*, 134114. DOI: 10.1063/1.2715585
- (59) Barbatti, M.; Aquino, A. J. A.; Lischka, H. The UV absorption of Nucleobases: Semi-Classical *Ab Initio* Spectra Simulations. *Phys. Chem. Chem. Phys.* **2010**, *12*, 4959-4967. DOI: 10.1039/B924956G
- (60) Crespo-Otero, R.; Barbatti, M. Spectrum Simulation and Decomposition with Nuclear Ensemble: Formal Derivation and Application to Benzene, Furan and 2-Phenylfuran. *Theor. Chem. Acc.* **2012**, *131*, 1237. DOI: 10.1007/s00214-012-1237-4
- (61) Bowman, J. M.; Gazdy, B.; Sun, Q. A Method to Constrain Vibrational Energy in Quasiclassical Trajectory Calculations *J. Chem. Phys.* **1989**, *91*, 2859-2862. DOI: 10.1063/1.456955
- (62) Guo, Y.; Thompson, D. L.; Sewell, T. D. Analysis of the Zero-Point Energy Problem in Classical Trajectory Simulations *J. Chem. Phys.* **1996**, *104*, 576-582. DOI: 10.1063/1.470853
- (63) Martínez-Fernández, L.; Corral, I.; Granucci, G.; Persico, M. Competing Ultrafast Intersystem Crossing and Internal Conversion: A Time Resolved Picture for the Deactivation of 6-Thioguanine. *Chem. Sci.* **2014**, *5*, 1336-1347. DOI: 10.1039/c3sc52856a
- (64) Kochman, M. A.; Pola, M.; Miller, R. J. D. Theoretical Study of the Photophysics of 8-Vinylguanine, an Isomorphous Fluorescent Analogue of Guanine. *J. Phys. Chem. A* **2016**, *120*, 6200-6215. DOI: 10.1021/acs.jpca.6b04723
- (65) Martin, R. L. Natural Transition Orbitals. *J. Chem. Phys.* **2003**, *118*, 4775-4777. DOI: 10.1063/1.1558471

- (66) Harman, P. J.; Kent, J. E.; O'Dwyer, M. F.; Smith, M. H. Quartz Ultraviolet Rydberg Transitions in Benzene Isomers. *Aust. J. Chem.* **1979**, *32*, 2579-2587. DOI: 10.1071/CH9792579
- (67) Dreyer, J.; Klessinger, M. Excited States and Photochemical Reactivity of Fulvene. A Theoretical Study. *J. Chem. Phys.* **1994**, *101*, 10655-10665 DOI: 10.1063/1.467879
- (68) De Vetta, M.; González, L.; Corral, I. The Role of Electronic Triplet States and High-Lying Singlet States in the Deactivation Mechanism of the Parent BODIPY: An ADC(2) and CASPT2 Study. *Chem. Photo. Chem.* **2018**, *2*. DOI: 10.1002/cptc.201800169
- (69) Bearpark, M. J.; Bernardi, F.; Olivucci, M.; Robb, M. A.; Smith, B. R. Can Fulvene S_1 Decay Be Controlled? A CASSCF Study with MMVB Dynamics. *J. Am. Chem. Soc.* **1996**, *118*, 5254-5260. DOI: 10.1021/ja9542799
- (70) Sicilia, F.; Bearpark, M. J.; Blancafort, L.; Robb, M. A. An Analytical Second-Order Description of the S_0/S_1 Intersection Seam: Fulvene Revisited. *Theor. Chem. Acc.* **2007**, *118*, 241-251. DOI: 10.1007/s00214-007-0320-8
- (71) Mendive-Tapia, D.; Lasorne, B.; Worth, G. A.; Bearpark, M. J.; Robb, M. A. Controlling the Mechanism of Fulvene S_1/S_0 Decay: Switching Off the Stepwise Population Transfer. *Phys. Chem. Chem. Phys.* **2010**, *12*, 15725-15733. DOI: 10.1039/C0CP01757D
- (72) Atchity, G. J.; Xantheas, S. S.; Ruedenberg, K. Potential Energy Surfaces Near Intersections. *J. Chem. Phys.* **1991**, *95*, 1862-1876. DOI: 10.1063/1.461036
- (73) Druzhinin, S. I.; Galievsky, V. A.; Yoshihara, T.; Zachariasse, K. A. Intramolecular Charge Transfer and Dielectric Solvent Relaxation in *n*-Propyl Cyanide. *N*-Phenylpyrrole and 4-Dimethylamino-4'-cyanostilbene. *J. Phys. Chem. A* **2006**, *110*, 12760-12768. DOI: 10.1021/jp0652547

- (74) Druzhinin, S. I.; Kovalenko, S. A.; Senyushkina, T. A.; Demeter, A.; Machinek, R.; Noltemeyer, M.; Zachariasse, K. A. Intramolecular Charge Transfer with the Planarized 4-Cyanofluorazene and Its Flexible Counterpart 4-Cyano-*N*-phenylpyrrole. Picosecond Fluorescence Decays and Femtosecond Excited-State Absorption. *J. Phys. Chem. A* **2008**, *112*, 8238-8253. DOI: 10.1021/jp8037413
- (75) Druzhinin, S. I.; Kovalenko, S. A.; Senyushkina, T. A.; Demeter, A.; Zachariasse, K. A. Intramolecular Charge Transfer with Fluorazene and *N*-Phenylpyrrole. *J. Phys. Chem. A* **2010**, *114*, 1621-1632. DOI: 10.1021/jp909682p



Supporting Information for

A Theoretical Study of Ground- and Excited-State
Charge Transfer in Fulvene-Based Donor-Acceptor
Systems

Michał Andrzej Kochman,[†] Bo Durbeej[†]

[†] Division of Theoretical Chemistry, Department of Physics, Chemistry and Biology (IFM), Linköping University, 581 83 Linköping, Sweden.

e-mail: michal.kochman@liu.se, bodur@ifm.liu.se

Contents

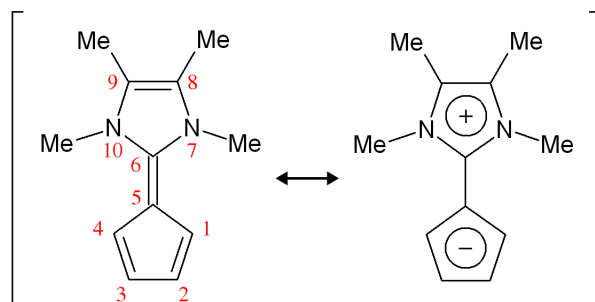
S1 Ground-State Electronic Structure of Compound II	S3
S2 Rydberg-type Excited States of Compound II	S6
S3 Optimization of the MCI of compound III at the XMS-CASPT2 Level	S9
S4 Photophysics of Compound II in Polar Solution	S11
S4.1 Electronic Excitation Spectrum	S11
S4.2 Potential Energy Surfaces	S12
S4.3 Molecular Electrostatic Potential	S13
S4.4 Relaxation Dynamics	S17
S4.4.1 Construction of Potential Energy Surfaces	S17
S4.4.2 Initial Conditions	S20
S4.4.3 Nonadiabatic Molecular Dynamics	S21
S4.4.4 Results and Discussion	S22
S5 Molecular Geometries	S25
References	S30

S1 Ground-State Electronic Structure of Compound **II**

As a preliminary to the present study, we characterized the ground-state electronic structure of compound **II**. In particular, we sought to quantify the zwitterionic character of compound **II**, and to answer the question of whether either (or both) of its five-membered rings can be considered as aromatic.

For ease of reference, the molecular structure and atom numbering of compound **II** is reproduced in Figure S1 below.

Figure S1: Molecular structure of compound **II**.

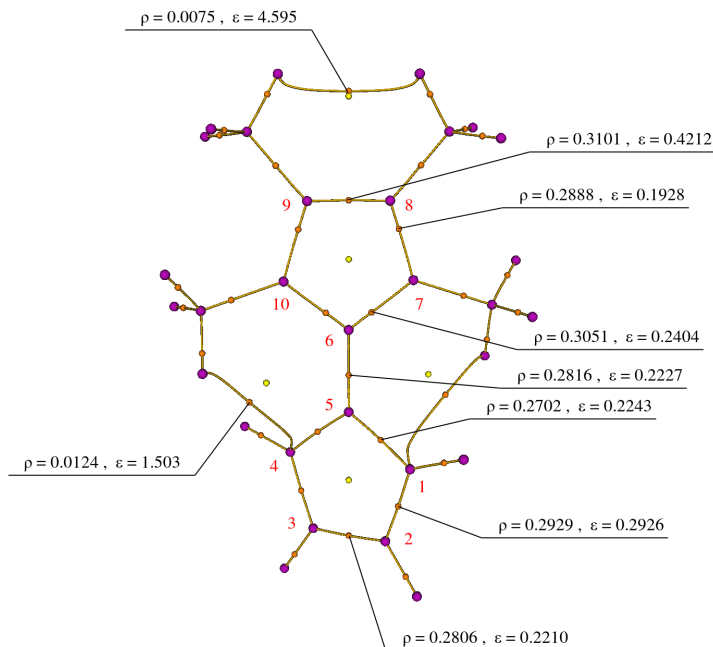


Chemical bonding in the ground electronic state of compound **II** was analyzed with the use of the descriptors introduced by the quantum theory of atoms in molecules (QTAIM) of Bader and coworkers.¹ (See Ref.² for an accessible exposition of the fundamental concepts of QTAIM.) The QTAIM analysis was performed with the computational chemistry software package Gaussian 09, Revision D.01,³ as well as with the program Multiwfn, version 3.5,^{4,5} which contains an interface to Gaussian 09. In all cases, the analysis was performed for the relaxed MP2/cc-pVDZ electron density.

The sum of atomic charges in the cyclopentadienyl moiety (i.e., carbons C1 to C5 and their hydrogen atoms) is $-0.37 e$, which confirms that compound **II** has partial zwitterionic character. However, it is not a fully formed zwitterion, as the total of atomic charges on the cyclopentadienyl moiety is significantly less than the electron charge.

Figure S2 shows the molecular graph (a plot of all critical points and bond paths) of compound **II**. The bonding within the conjugated π -bonding system is further characterized by indicating the electron density (ρ_{BCP} , in units of e/a_0^3) of the relevant bond critical points (BCPs), as well as their ellipticities (ε). This data is again consistent with the interpretation that compound **II** has only partial zwitterionic character: the C1–C2 and C3–C4 bonds are slightly shorter than the other three bonds in the cyclopentadienyl ring and, what is more, the BCPs along the bond paths of the C1–C2 and C3–C4 bonds exhibit markedly higher ellipticities than the BCPs along the other three bonds in that ring. In contrast, in a fully formed zwitterion, all five bonds in the cyclopentadienyl moiety would be expected to have near-identical properties.

Figure S2: Molecular graph of compound **II** showing nuclear critical points (violet), bond critical points (BCPs, orange), and ring critical points (RCPs, yellow). Bond paths are marked in beige. ρ is the electron density at a given BCP in units of e/a_0^3 , and ε is its ellipticity. Atom numbering is given in red.

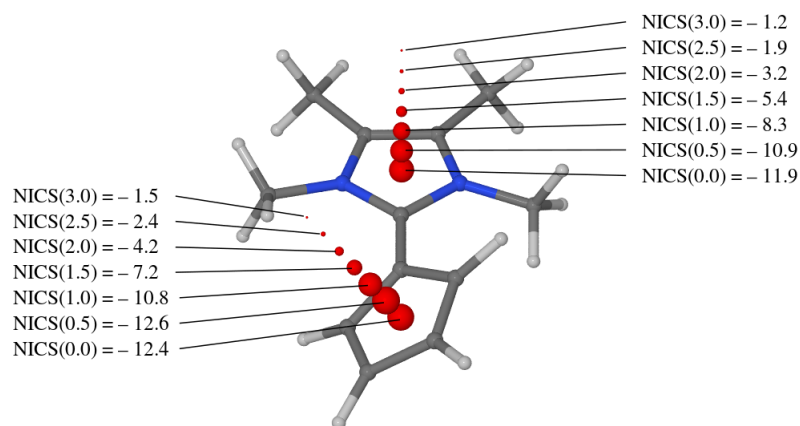


Interestingly, the QTAIM analysis also provides evidence for charge-assisted hydrogen bonds (CAHBs) between carbon atom C1 (and C4), and the closest hydrogen atom of the methyl group at nitrogen atom N7 (and N10). Namely, a bond path is detected that connects the nucleus of atom C1, and the closest proton of the methyl group at atom N7. Another bond path, related to first by symmetry, connects the nucleus of atom C4 and the closest proton of the methyl group at atom N10. The electron density at the BCP along either paths takes a low value of $0.0124 e/a_0^3$, whereas the Laplacian of the electron density is positive. This indicates that the underlying bonding interactions are weak and closed-shell in nature. On the basis of the above, we identify these interactions as CAHBs between the methyl group hydrogens, and the carbon atoms of the cyclopentadienyl ring. This interpretation is supported by reference to previous studies which have identified instances of carbon-bonded hydrogen atoms forming CAHBs with the cyclopentadienyl anion.^{6–9}

A bond path is also located between a proton of the methyl group at atom C8, and its symmetry counterpart in the methyl group at atom C9. The electron density at the BCP along that bond path is very low, however, which rules out a significant bonding interaction between these two hydrogens.

As expected, a ring critical point (RCP) is found in the interior of the tetramethylimidazolium ring, and another in the cyclopentadienyl ring. Two more RCPs are located in the regions to either side of the central C5–C6 bond. Lastly, a fifth RCP is found in the volume of space enclosed by the methyl groups bonded to atoms C8 and C9.

Figure S3: The NICS(x) indices (expressed as ppm) computed at and above the RCPs of compound **II**. The red spheres indicate the points where the NICS(x) index was calculated, and their diameters are proportional to the local NICS values.



Finally, we undertook to answer the question of whether either or both of the five-membered rings of compound **II** can be considered to be aromatic. We elected to quantify aromaticity on the basis of the nucleus-independent chemical shift (NICS) index.¹⁰ In line with the usual convention, we defined the NICS(x) index as the negative of the magnetic shielding, calculated at a point located at a distance of x ångström from the RCP of the given ring, along a line perpendicular to a plane least-square-fitted to that ring. The magnetic shielding was computed with at the MP2/cc-pVDZ level of theory in combination with the gauge-independent atomic orbital (GIAO) method.^{11–15} The calculation was performed in Gaussian 09.

The resulting NICS(x) values are shown in Figure S3 above. The NICS(x) index at, and above, the RCP of the cyclopentadienyl ring takes appreciably negative values, which demonstrates the presence of induced diatropic ring currents. Likewise, the NICS(x) index at and above the RCP of the tetramethylimidazolium ring also adopts negative values. It follows that both of the five-membered rings of compound **II** can be considered as aromatic.

S2 Rydberg-type Excited States of Compound II

Although the present study revolves around the valence excited states of compound **II**, it is also of some interest to characterize its Rydberg-type states. To this end, we recalculated the vertical excitation spectrum of compound **II**, using, once again, the ADC(2) method, but now in combination with the r-aug-cc-pVDZ (“reduced aug-cc-pVDZ”) basis set defined in Ref.¹⁶ The r-aug-cc-pVDZ basis set is derived from the standard aug-cc-pVDZ basis set by deleting the diffuse d subshell on the heavy atoms, as well as the diffuse p subshell on the hydrogens. Thus, the diffuse functions retained in the basis set are the diffuse s and p functions on the heavy atoms, and the diffuse s functions on the hydrogens. The default auxiliary basis set for aug-cc-pVDZ was used as the auxiliary basis set for r-aug-cc-pVDZ.

The results of this calculation are summarized in Table S1 below. Accompanying this data, Figure S4 shows the natural transition orbitals (NTOs) for transitions from the S_0 state. It can be seen that the lowest $\pi\pi^*$ -type states of compound **II** are embedded in a manifold of Rydberg-type states; in fact, the calculation places the lowest Rydberg-type state (i.e., the $1^1B \pi R$ state) below the lowest valence state (the $2^1A \pi\pi^*$ state). Inspection of the corresponding NTOs reveals that the low-lying Rydberg-type states arise from the excitation of an electron from a π -type valence orbital into a diffuse volume of space enveloping the tetramethylimidazolium moiety. Accordingly, we label these states as πR states.

What is more, the S_2 ($2^1A \pi\pi^*$) and S_4 ($2^1B \pi\pi^*$) states, though mainly valence in character, exhibit an admixture of Rydberg character. This is evidenced by the fact that the NTOs for transitions into these states from the S_0 state show partial diffuse character, mainly around the methyl groups bonded to atoms N7 and N10.

Now, it is well documented that the ADC(2) method, and also the closely related second-order approximate coupled cluster^{17–19} (CC2) method, systematically

Table S1: Vertical excitation spectrum of compound **II** calculated at the ADC(2)/r-aug-cc-pVDZ level of theory: vertical excitation energies (ΔE) and associated oscillator strengths (f). The calculation was performed at the S_0 -min geometry optimized at the MP2/r-aug-cc-pVDZ level of theory.

State	ΔE , eV	f	μ , D ^a
S_0 (1^1A)			8.69
S_1 ($1^1B \pi R$)	3.493	0.003	−2.75
S_2 ($2^1A \pi\pi^*$)	3.756	0.467	5.40
S_3 ($3^1A \pi R$)	3.852	0.029	−0.71
S_4 ($2^1B \pi\pi^*$)	3.948	0.008	2.28
S_5 ($4^1A \pi R$)	4.038	0.026	−1.55
S_6 ($3^1B \pi R$)	4.178	0.004	1.44

^a μ is the magnitude of the (orbital-relaxed) electric dipole moment of a given electronic state; a negative value indicates that its direction is antiparallel to the electric dipole moment of the S_0 state.

underestimate excitation energies into Rydberg-type states.^{16,20,21} The error with reference to higher-level methods is typically of the order of a few tenths of an eV. Thus, it is likely that in reality, the lowest Rydberg-type states lie slightly higher in energy than the lowest $\pi\pi^*$ -type states. However, even allowing for this systematic error of ADC(2), it is clear that compound **II** possesses a manifold of low-lying Rydberg-type states.

The reason for the appearance of low-energy Rydberg-type states is that the valence electrons of compound **II** are rather weakly bound. More formally, the vertical ionization potential (VIP) of compound **II** is unusually low for an organic molecule. A calculation of the VIP at the density functional theory (DFT) level, using the M06-2X functional²² in combination with the def2-TZVP basis set,²³ gives a value of 6.358 eV.

A rough estimate of the VIP may also be obtained by referring to Koopmans' theorem,²⁴ according to which the VIP is equal to the negative of the orbital energy of the highest occupied molecular orbital of the neutral species. A Koopmans' theorem calculation based on the RHF/cc-pVDZ orbital energies yields a value of 6.399 eV, which coincides closely with the prediction of the much more reliable DFT-based approach.

The change in electron density upon ionization was characterized with the use of the electron density difference map (EDDM), which is defined simply as the difference of the electron density of the ionized state and that of the neutral ground state at the same nuclear geometry. The EDDM for the vertical ionization of compound **II** is plotted in Figure S5. It can be seen that the electron density is mainly removed from atom C5 and the π -bonding regions of the C2–C3 and C8–C9 bonds.

Figure S4: Dominant NTOs for vertical excitations of compound **II**, obtained at the ADC(2)/r-aug-cc-pVDZ level of theory, plotted in the form of isosurfaces with isovalues of $\pm 0.02 a_0^{-3/2}$. The eigenvalue (λ_i) for each occupied-virtual NTO pair is given in terms of a percentage contribution.

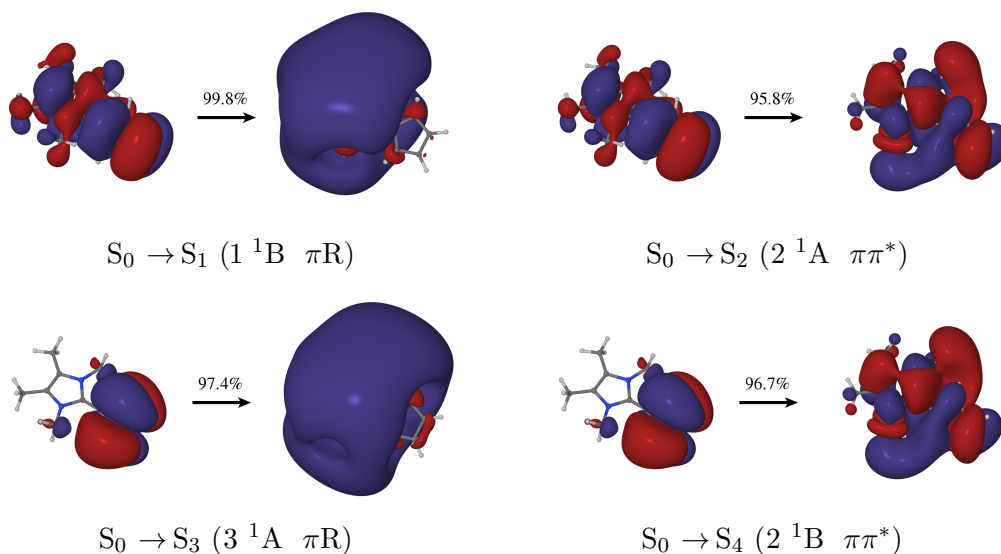
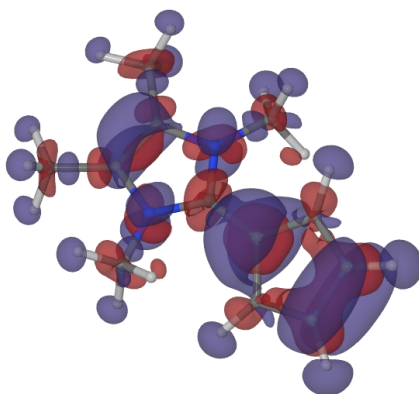


Figure S5: EDDM for vertical ionization of compound **II**, plotted in the form of isosurfaces with isovalues of $\pm 0.002 e/a_0^3$. The semitranslucent red and blue isosurfaces delimit regions in which the electron density is increased and decreased, respectively, upon vertical ionization. The calculation was performed at the M06-2X/def2-TZVP level of theory.



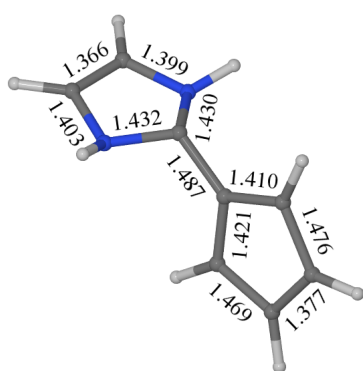
S3 Optimization of the MCI of compound **III** at the XMS-CASPT2 Level

In the present section, we discuss the optimization of the minimum-energy S_1/S_0 conical intersection (MCI) of compound **III** at the XMS-CASPT2 level of theory. In the course of the optimization, a SA-2-CASSCF reference was used. The remaining simulation parameters were the same as previously specified in Section 2.1 of the main body of this paper.

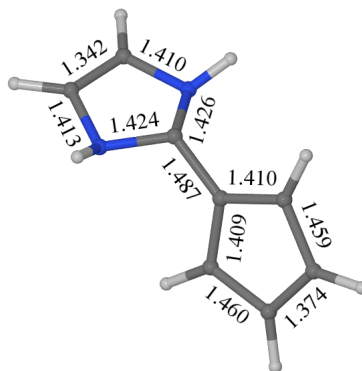
The resulting MCI geometry is illustrated in Figure S6 (a). For ease of reference, the MCI geometry obtained previously at the CASSCF level is shown in Figure S6 (b). As expected, there are some minor differences in terms of bond lengths between the two structures. Notably, XMS-CASPT2 predicts a more pronounced elongation of the C1-C2 and C3-C4 bonds than does CASSCF. However, when it comes to the overall conformation of the molecular skeleton, CASSCF is in close agreement with the benchmark provided by XMS-CASPT2. This point is illustrated in Figure S7, where the structures obtained with XMS-CASPT2 and CASSCF are overlaid on one another. (The XMS-CASPT2- and CASSCF-optimized geometries are drawn in blue and red, respectively.)

The reasonably good agreement between the MCI geometries obtained with XMS-CASPT2 and CASSCF indicates that the latter method achieves a satisfactorily realistic description of the S_1/S_0 conical intersection seam. Accordingly, in the calculations reported in the main body of this paper, we rely on the computationally less demanding CASSCF method.

Figure S6: Molecular geometry at the S_1/S_0 MCI of compound **III** as optimized at the (a) XMS-CASPT2/cc-pVDZ and (b) CASSCF/cc-pVDZ level of theory.

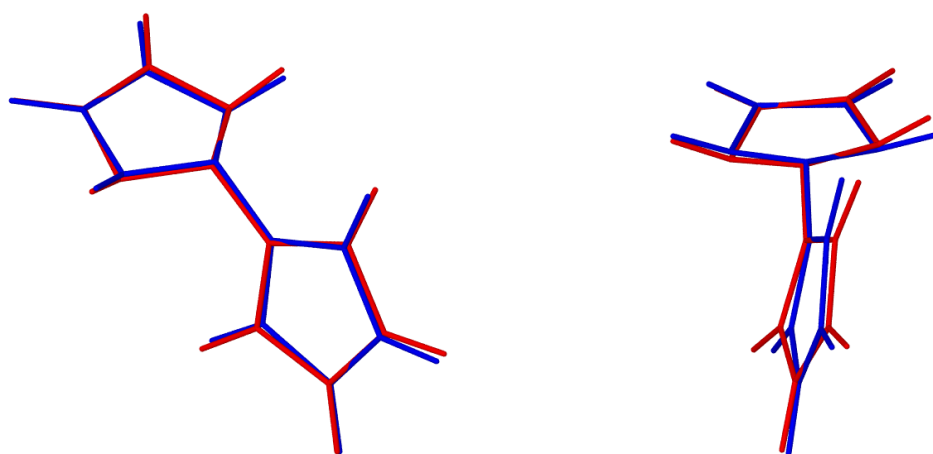


(a) XMS-CASPT2/cc-pVDZ



(b) CASSCF/cc-pVDZ

Figure S7: A visual comparison of the MCI geometries obtained with XMS-CASPT2 (drawn in blue) and CASSCF (red). The two geometries have been overlaid on one another in such a way as to minimize the root-mean-square deviation between atomic positions. The panels of this Figure show the overlay from two different perspectives.



S4 Photophysics of Compound II in Polar Solution

A Reviewer asked the insightful question of how the photophysics of compound **II** is affected by aqueous solvation. In order to answer that question, we performed some additional simulations which addressed solvent effects in the electronic excitation spectrum of compound **II** and in its excited-state relaxation dynamics. Here, we provide a summary of our findings in this regard.

S4.1 Electronic Excitation Spectrum

We focus firstly on the electronic excitation spectrum of compound **II**. Solvent effects were taken into account by recalculating the vertical excitation spectrum at the ADC(2)/cc-pVDZ level of theory in combination with the conductor-like screening model^{25,26} (COSMO) implemented in Turbomole 7.0.²⁷ COSMO is an implicit solvation model in which solvation is represented by placing the molecule in a cavity within a polarizable continuum.

Because the COSMO model is only implemented for single-point calculations, the calculation of the vertical excitation spectrum was performed at the MP2/cc-pVDZ geometry optimized *in vacuo*.

Aqueous solvation was represented by setting the dielectric constant of the environment as $\epsilon=80.0$ and the refractive index as $n=1.3$. Nonequilibrium solvation was imposed when calculating the vertical excitation energies, which is to say that the slow part of the reaction field was equilibrated with the initial state (S_0), while the fast electronic part of the reaction field was equilibrated with the target excited state. (The reaction field is the electrostatic field generated by the implicit solvent.) The cavity around the molecule was constructed using the standard solvent accessible surface scheme using the optimized atomic COSMO radii ($r_C=2.00$ Å, $r_N=1.83$ Å, $r_H=1.30$ Å) and a solvent radius of $r_{\text{solv}}=1.30$ Å. Program defaults were used for the remaining adjustable parameters.

The results are summarized in Table S2. For reference, Table S2 also lists the results of the gas-phase ADC(2)/cc-pVDZ calculations reported previously in Table 1 in the main body of this paper. Aqueous solvation causes an upward (blue) shift in the vertical excitation energies into the S_1 (2^1A) and S_2 (1^1B) states, the latter being more affected than the former. This can be explained by the fact that the S_0 state is strongly polar (zwitterionic), whereas the S_1 (2^1A) is only weakly polar, and the S_2 (1^1B) state is essentially nonpolar. Immediately following vertical excitation, the slow part of the reaction field remains in equilibrium with the polar ground state. Therefore, it destabilizes both of the low-lying excited states, but especially the S_2 (1^1B) state.

The S_3 state and all higher singlet excited states of compound **II** in aqueous solution remain well separated from the S_1 and S_2 states, and they are not expected to be involved in the relaxation dynamics of this compound following the irradiation of the first photoabsorption band.

Table S2: A comparison of the vertical excitation spectra of compound **II** in the gas phase and in aqueous solution: vertical excitation energies (ΔE) and associated oscillator strengths (f). The calculation was performed at the ADC(2)/cc-pVDZ level of theory at the gas-phase equilibrium geometry, optimized at the MP2/cc-pVDZ level.

Environment	State	ΔE , eV	f	μ , D ^a
Gas phase	S ₀ (1 ¹ A)			8.31
	S ₁ (2 ¹ A)	3.909	0.541	5.77
	S ₂ (1 ¹ B)	4.089	0.012	2.02
	S ₃ (2 ¹ B)	5.095	0.057	-2.78
Aqueous solution	S ₀ (1 ¹ A)			12.05
	S ₁ (2 ¹ A)	4.138	0.619	9.02
	S ₂ (1 ¹ B)	4.678	0.023	5.34
	S ₃ (2 ¹ B)	5.861	0.076	2.94

^a μ is the magnitude of the (orbital-relaxed) electric dipole moment of a given electronic state; a negative value indicates that its direction is antiparallel to the electric dipole moment of the S₀ state.

S4.2 Potential Energy Surfaces

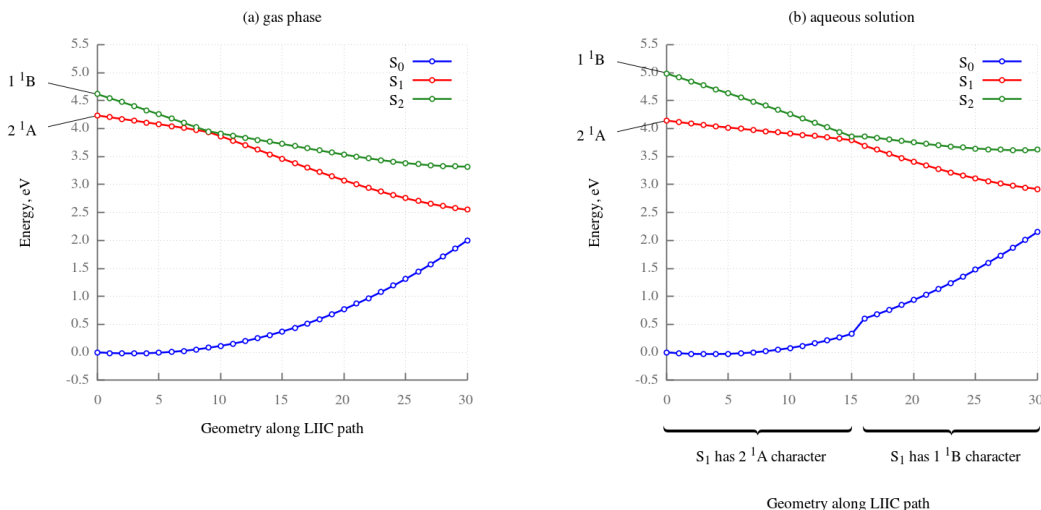
As we have seen in the previous subsection, aqueous solvation causes a blue-shift in the vertical excitation energies into the low-lying singlet excited states of compound **II**. It may also affect the topography of the excited-state potential energy surfaces (PESs). In order to explore this possibility, we performed a scan of the relevant PESs, again using the COSMO solvent model.

At this stage, we resorted to performing the calculations on compound **III**, which is the size-reduced model of the larger compound **II**. The calculations were performed at the ADC(2) level of theory along the reaction path generated in Section 3.3 in the main body of this paper. The starting point of the reaction path is the ground-state equilibrium geometry of compound **III** as optimized at the SA-2-CASSCF(12,10)/cc-pVDZ level of theory. The end point is the geometry of the MCI along the S₁/S₀ conical intersection seam, optimized at the same level of theory. The intermediate geometries were generated by means of linear interpolation in internal coordinates (LIIC) between these two structures.

The potential energy surfaces were calculated at the ADC(2)/cc-pVDZ level with the solvent being treated by means of the COSMO model. It was assumed that the solvent is in equilibrium with the S₁ adiabatic state at all times. The energies of the other states were calculated using the nonequilibrium approach.

Figure S8 compares the topography of the PESs in vacuum (panel (a)) and in aqueous solution (panel (b)). It can be seen that aqueous solvation destabilizes the nonpolar 1 ¹B diabatic state relative to the moderately polar 2 ¹A diabatic state. Figuratively speaking, in Figure S8 (b), the curve of the 1 ¹B state is “lifted” upwards in energy with respect to the 2 ¹A state.

Figure S8: Energies of singlet electronic states of compound **III** along the LIIC path from the Franck-Condon geometry to the MCI geometry, calculated (a) in the gas phase and (b) in aqueous solution. The calculations were performed at the ADC(2)/cc-pVDZ level of theory. (Panel (a) shows the same data as Figure 7 (c) in the main body of this paper.)



In the solution-phase PES scan, there is a prominent “jump” in the potential energy curve of the S_0 state on going from the 15th interpolated geometry to the 16th. Careful inspection reveals that there is also a smaller “jump” in the potential energy curve of the S_2 state. The reason for these sudden changes in the potential energy curves is that the system traverses a crossing between the S_2 and S_1 states. While this happens, the diabatic character of the S_1 state, with which the reaction field is equilibrated, changes sharply from $2\ ^1A$ to $1\ ^1B$. As a consequence, there is a sudden change in the reaction field, and the energies of the other states change rapidly.

Due to the close structural similarity between compounds **II** and **III**, the conclusion that aqueous solvation destabilizes the $1\ ^1B$ state relative to the $2\ ^1A$ state can be extrapolated to compound **II**. This effect is expected to reduce the accessibility of the S_1/S_0 conical intersection seam, where the S_1 state has $1\ ^1B$ diabatic character. It follows that the excited-state lifetime of compound **II** will most likely be somewhat longer in aqueous solution than in the gas phase.

S4.3 Molecular Electrostatic Potential

On the subject of solvent effects in the relaxation dynamics of compound **III**, it is worthwhile to examine the molecular electrostatic potential^{28,29} (MEP) generated by each of the relevant states. Owing to the fact that the MEP reflects the local balance of nuclear and electronic charge, it provides a useful visual indication of the polarity of a given electronic state. Furthermore, the MEP plays a special role in intermolecular interactions, such as, for example, solvent-solute interactions. In

polarization theory,^{30,31} which is the most basic application of Rayleigh-Schrödinger perturbation theory to the problem of weak (noncovalent) interactions, the first-order term in the perturbation expansion of the interaction energy takes the form of the electrostatic interaction between the charge distributions of the two interacting systems:

$$E_{\text{pol}}^{(1)} = \int \int \rho_{\text{A}}(\mathbf{r}_1) \frac{1}{r_{12}} \rho_{\text{B}}(\mathbf{r}_2) d\mathbf{r}_1 d\mathbf{r}_2 \quad (1)$$

Here, $\rho_{\text{A}}(\mathbf{r})$ and $\rho_{\text{B}}(\mathbf{r})$ are the total charge distributions of the interacting systems A and B. Equation 1 can equivalently be interpreted as the total charge density of one system being subjected to the MEP generated by the other system.

The MEPs generated by the the ground- and excited states of compound **II** were calculated on the basis of orbital-relaxed MP2/cc-pVDZ and ADC(2)/cc-pVDZ densities. These calculations were performed with the use of the following algorithm, implemented in an external program. Let us recall that the MEP generated by a molecule at a point \mathbf{r} is given rigorously by the following expression:

$$V(\mathbf{r}) = \sum_I \frac{Z_I}{|\mathbf{R}_I - \mathbf{r}|} - \int \frac{\rho(\mathbf{r}')}{|\mathbf{r}' - \mathbf{r}|} d\mathbf{r}' \quad (2)$$

where $\rho(\mathbf{r})$ is the electron density, and \mathbf{R}_I and Z_I are, respectively, the position of the I -th nucleus and its charge.

For each electronic state of interest, the electronic density was represented on a uniformly spaced three-dimensional grid $\{\mathbf{r}_{i,j,k}\}$. As illustrated schematically in Figure S9, the approximation was made that each grid point was considered to be the center of a cubic voxel (volume element) in which the electronic density was treated as uniform. Thus, the integral which appears in equation 1 was approximated as a sum of contributions from the individual uniformly charged voxels:

$$V(\mathbf{r}) = \sum_I \frac{Z_I}{|\mathbf{R}_I - \mathbf{r}|} - \sum_{i,j,k} \rho(\mathbf{r}_{i,j,k}) \int_{V_{i,j,k}} \frac{1}{|\mathbf{r}' - \mathbf{r}|} d\mathbf{r}' \quad (3)$$

The integral

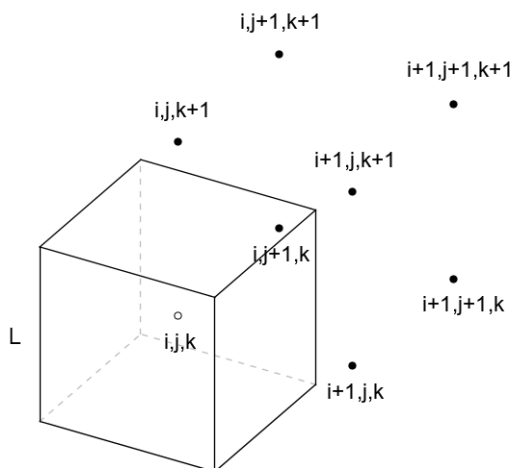
$$\int_{V_{i,j,k}} \frac{1}{|\mathbf{r}' - \mathbf{r}|} d\mathbf{r}' \quad (4)$$

represents the electrostatic potential generated by the uniformly charged cubic voxel centered at the grid point $\mathbf{r}_{i,j,k}$. These integrals were evaluated using the analytic expression for the electrostatic potential of a uniformly charged cube given by Hummer.^{32,33} The exact result for $V(\mathbf{r})$ is recovered in the limit of infinitesimal grid spacing. In practice, we have found that for molecules containing only hydrogen and second-row elements, the MEP is essentially converged with respect to the grid spacing at $L = 0.03$ Å. Hence, that value of L was applied in all calculations.

In order to achieve a saving of computing time, $V(\mathbf{r})$ was evaluated on the same grid that was used to represent the electron density. This made it possible to tabulate values of the integral given in expression 4 for different values of $\mathbf{r} - \mathbf{r}_{i,j,k}$, and reuse them during the calculation.

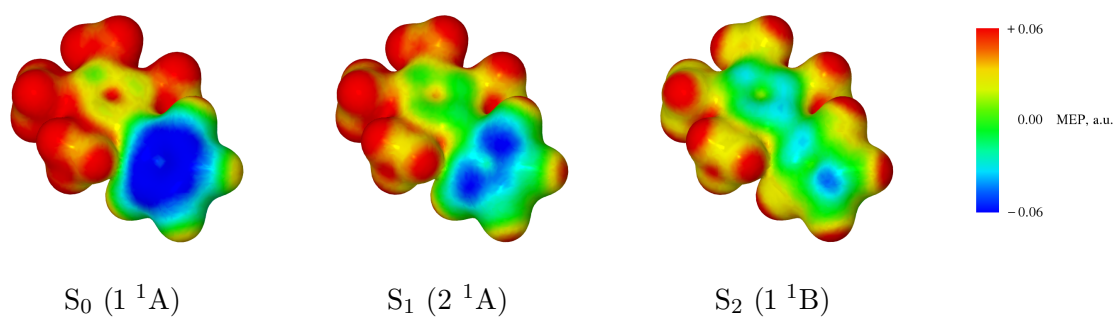
The results are plotted in Figure S10. The MEP generated by the S_0 (1^1A) state

Figure S9: Schematic illustration of the approximation made when computing the MEP. The electron density $\rho(\mathbf{r})$ is given on a uniformly spaced three-dimensional grid. Each grid point $\mathbf{r}_{i,j,k}$ identified by indices i, j, k is considered to be the center of a cubic voxel (denoted $V_{i,j,k}$) whose side length L is the same as the grid spacing, and whose edges are parallel to the grid directions. During the calculation of the MEP, the electron density within the voxel is treated as constant and equal to the electron density value at the grid point.



clearly reflects its partial zwitterionic character: the negatively charged cyclopentadienyl moiety is flanked by volumes of markedly negative potential, whereas the positively charged tetramethylimidazolium moiety is enveloped in a volume of positive potential. The S_1 (2^1A) state is markedly less polar than the ground state. Lastly, the S_2 (1^1B) state is essentially nonpolar – in that state, both ends of the molecule are electrically close to neutral. This latter observation explains why polar solvation causes a large blue shift of the vertical excitation energy into the S_2 (1^1B) state.

Figure S10: Plots of the MEP generated by compound **II** in its ground and excited electronic states. For each state, the MEP is projected onto the $0.01\ e/a_0^3$ isodensity surface of that state. Areas of negative and positive MEP appear in blue and red, respectively.



S4.4 Relaxation Dynamics

Our next order of business will be to examine solvent effects in the relaxation process that is triggered by the irradiation of the lowest photoabsorption band of compound **II** in aqueous solution. In order to capture the simultaneous dynamics of the solute and the solvent, we decided to perform a set of nonadiabatic dynamics simulations using an explicit solvent model.

S4.4.1 Construction of Potential Energy Surfaces

The PESs of the system were constructed with the use of the hybrid quantum mechanics/molecular mechanics³⁴⁻³⁶ (QM/MM) method. Within the framework of that method, the system under study (denoted \mathbb{S}) is partitioned into subsystems that are treated at different levels of approximation. The electronic structure of the so-called inner subsystem (\mathbb{I}) is explicitly included in the simulation, and it is calculated with the use of a quantum-mechanical (QM) method. In turn, the outer subsystem (\mathbb{O}) is described with a molecular mechanics (MM) force field.

In the present case, the natural choice of QM/MM partitioning is that the solute molecule is included in the inner subsystem, and the surrounding water molecules comprise the outer subsystem. This simulation setup is shown schematically in Figure S11. Because periodic boundary conditions are not available in Turbomole, in our simulations the solution phase was represented by placing the solute molecule at the center of a water droplet containing 600 water molecules.

We elected to employ the additive variant³⁶ of the QM/MM method. In this approach, the potential energy function ($E_{\text{QM/MM}}(\mathbb{S})$) of the system is broken down as follows:

$$E_{\text{QM/MM}}(\mathbb{S}) = E_{\text{QM}}(\mathbb{I}) + E_{\text{MM}}(\mathbb{O}) + E_{\text{QM-MM}}(\mathbb{I}, \mathbb{O}) \quad (5)$$

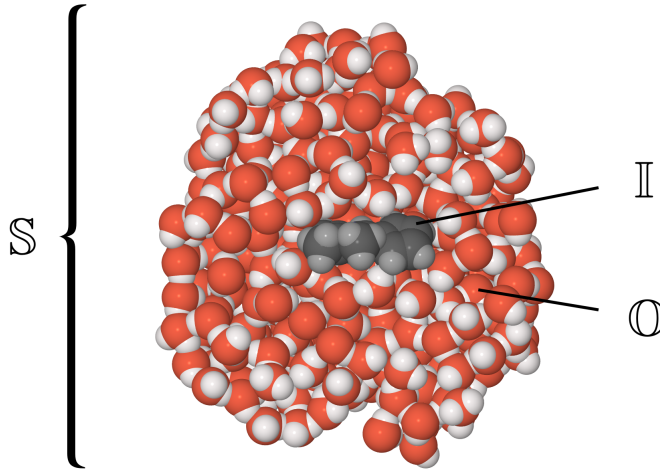
Here, $E_{\text{QM}}(\mathbb{I})$ represents the energy of the inner subsystem calculated at the QM level of theory. In turn, $E_{\text{MM}}(\mathbb{O})$ is the energy of the outer subsystem, evaluated at the MM level of theory. Lastly, $E_{\text{QM-MM}}(\mathbb{I}, \mathbb{O})$ is the QM-MM coupling term, whose purpose is to account for the interactions between the inner and outer subsystems.

In the present implementation, the inner and outer subsystems interact via electrostatic and Van der Waals interactions. The electrostatic interactions are handled with the use of the electrostatic embedding scheme,³⁶ whereby the QM calculation for the inner subsystem is performed in the presence of the charge distribution of the outer subsystem. More specifically, the point charges of the MM force field are included in the QM Hamiltonian. This allows the electronic structure of the inner subsystem to adapt to the charge distribution of its environment. Because the electrostatic part of the interaction between the inner and outer subsystems is calculated during the QM calculation, it is subsumed into the term E_{QM} , which becomes a function of \mathbb{O} in addition to being a function of \mathbb{I} . As a consequence, equation 5 takes on a modified form:

$$E_{\text{QM/MM}}(\mathbb{S}) = E_{\text{QM}}(\mathbb{I}, \mathbb{O}) + E_{\text{MM}}(\mathbb{O}) + E_{\text{QM-MM}}(\mathbb{I}, \mathbb{O}) \quad (6)$$

As in the gas-phase simulations, the electronic structure of the compound **II** (more specifically, the term $E_{\text{QM}}(\mathbb{I}, \mathbb{O})$) was evaluated at the ADC(2)/cc-pVDZ level of theory.

Figure S11: Schematic illustration of the partitioning of the system (denoted \mathbb{S}) into the inner (\mathbb{I}) and outer (\mathbb{O}) subsystems. The image shows a cross-section of the water droplet solvating a molecule of compound **II**.



The energy of the solvent (namely, the term $E_{\text{MM}}(\mathbb{O})$) was described with the use of the flexible TIP3P (TIP3P/Fs) water model as parameterized by Schmitt and Voth.³⁸ Its functional form is as follows:

$$E_{\text{MM}}(\mathbb{O}) = \sum_{i,j \in \mathbb{O}}^{\text{bonds}} \frac{1}{2} k_{ij} (r_{ij} - r_{ij}^0)^2 + \sum_{i,j,k \in \mathbb{O}}^{\text{angles}} \frac{1}{2} k_{ijk} (\theta_{ijk} - \theta_{ijk}^0)^2 + \sum_{i,j \in \mathbb{O}}^{\text{inter}} \left\{ 4\varepsilon_{ij} \left[\left(\frac{\sigma_{ij}}{r_{ij}} \right)^{12} - \left(\frac{\sigma_{ij}}{r_{ij}} \right)^6 \right] + \frac{q_i q_j}{r_{ij}} \right\} \quad (7)$$

The first term on the right-hand side of equation 7 accounts for the stretching of O–H bonds, the second term describes the bending of the water molecule (the angle between the two O–H bonds), and the third term handles all water-water intermolecular interactions. The values of the interaction parameters are listed in Table S3.

The Van der Waals interactions between the inner and outer subsystems are retained in the QM-MM coupling term ($E_{\text{QM-MM}}(\mathbb{I}, \mathbb{O})$), and are modeled with the 6–12 Lennard-Jones potential:

$$E_{\text{QM-MM}}(\mathbb{I}, \mathbb{O}) = \sum_{i \in \mathbb{I}}^{\text{atoms}} \sum_{j \in \mathbb{O}}^{\text{atoms}} 4\varepsilon_{ij} \left[\left(\frac{\sigma_{ij}}{r_{ij}} \right)^{12} - \left(\frac{\sigma_{ij}}{r_{ij}} \right)^6 \right] \quad (8)$$

The van der Waals parameters for the atoms belonging to compound **II** were taken from the all-atom Optimized Potential for Liquid Simulations³⁷ (OPLS/AA) force field. The assignment of atom types is shown in Figure S12. All sp^2 -hybridized carbon atoms were considered to have the “alkene $\text{R}_2\text{-C=}$ ” atom type. The same van der Waals parameters were also used for the two sp^2 -hybridized nitrogen atoms of compound **II**. The four methyl group carbons were considered to have the “alkane $\text{CH}_3\text{-}$ ” atom type. Lastly, all hydrogen atoms were treated as the “alkane H-C ” atom type. The corresponding parameters from the OPLS/AA force field are listed

Figure S12: The assignment of MM atom types to atoms comprising compound **II**.

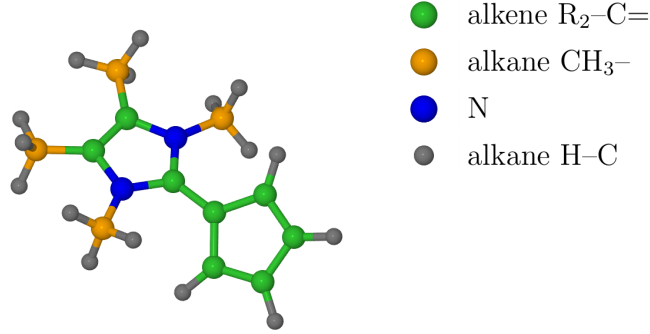


Table S3: Force field parameters used in the present study.

(a) Parameters for intermolecular interactions.^{37,38}

Atom type (i)	ε_{ii} , kcal/mol	σ_{ii} , Å	q , e
alkene $R_2-C=$	0.0760	3.5500	
alkane CH_3-	0.0660	3.5000	
N	0.0760	3.5500	
alkane $H-C$	0.0300	2.5000	
O (water)	0.1522	3.1506	-0.834
H (water)	0	N/A	+0.417

(b) Parameters for intramolecular interactions of TIP3P/Fs water.³⁸

$$\begin{aligned}
 k_{OH} &= 1059.162 \text{ kcal mol}^{-1} \text{ Å}^{-2} & r_{OH}^0 &= 0.96 \text{ Å} \\
 k_{HOH} &= 68.087 \text{ kcal mol}^{-1} \text{ rad}^{-2} & \theta_{HOH}^0 &= 104.5^\circ
 \end{aligned}$$

in the upper part of Table S3.

As is conventional in the OPLS/AA force field, the “mixed” interaction parameters σ_{ij} and ε_{ij} which appear in equation 8 were obtained with the use of geometric combining rules: $\sigma_{ij} = (\sigma_{ii}\sigma_{jj})^{1/2}$ and $\varepsilon_{ij} = (\varepsilon_{ii}\varepsilon_{jj})^{1/2}$.

In order to ensure that the water droplet remained roughly spherical in shape, and also to prevent the evaporation of the droplet, all atoms contained in the system were subjected to a harmonic spherical boundary potential:

$$V(\mathbf{R}) = \begin{cases} \frac{1}{2} k_B (|\mathbf{R}| - R_B)^2 & \text{if } |\mathbf{R}| - R_B > 0 \\ 0 & \text{otherwise} \end{cases} \quad (9)$$

The value of the force constant k_B was set to $0.5 \text{ kcal mol}^{-1} \text{ Å}^{-2}$.

S4.4.2 Initial Conditions

Following Ruckebauer and coworkers,^{39,40} when generating the initial conditions for the nonadiabatic molecular dynamics simulations, we adopted a hybrid procedure which treats the solute and solvent on a different footing. The positions and velocities of atoms comprising the solute molecule were selected in such a way as to include the zero-point energies of the intramolecular vibrational modes. The solvent was then thermalized in the presence of the solute. This approach is justified by the fact that the inclusion of zero-point energies in the intramolecular modes of the solute is required for a realistic calculation of spectral properties and relaxation dynamics.⁴¹ However, the TIP3P/Fs water model was parameterized for use in purely classical molecular dynamics simulations, and so the solvent must be treated entirely classically. The inclusion of zero-point energies in the solvent degrees of freedom is not desired.

Firstly, the ground-state equilibrium geometry of the compound **II** was optimized at the MP2/cc-pVDZ level of theory in vacuum. We remark here that using an equilibrium geometry optimized for the isolated molecule is only an approximation; we neglect the effect of aqueous solvation on the initial geometry of the solute. The reason that this approximation is necessary is that a geometry optimization and vibrational frequency calculation in the presence of solvent would have been prohibitively expensive in terms of computing time.

Phase space points (i.e. sets of nuclear positions and velocities) were sampled from the Wigner distribution of the ground-state equilibrium geometry. As noted in Refs.,^{42–44} semiclassical simulations of hydrogen-rich molecules are prone to an artificial leakage of zero-point energy from the stretching modes of hydrogen-heavy atom bonds to other vibrational modes. In order to mitigate this problem, when generating the Wigner distribution we froze the sixteen highest vibrational modes, which correspond to C–H modes.

Each of the molecular geometries sampled from the Wigner distribution was immersed in a water droplet consisting of 600 water molecules. Afterwards, the aqueous solvent was equilibrated with the solute by propagating a molecular dynamics trajectory in the canonical (NVT) ensemble. During the equilibration, the geometry of the solute was kept frozen, and the potential energy surface of the entire system was calculated with the MM method. The charge distribution of the solute was represented by a set of point charges placed at the nuclear positions. These were generated by fitting to the electrostatic potential generated by the relaxed MP2/cc-pVDZ electron density. The fit was performed with the use of the Merz-Singh-Kollman scheme⁴⁵ as implemented in the computational chemistry software package Gaussian 16, Revision B.01.⁴⁶ The temperature of the solvent was maintained at 298 K by applying the Langevin thermostat with a friction coefficient of $\gamma = 1$ ps. The Langevin equation of motion was propagated with the use of the Brünger-Brooks-Karplus (BBK) integrator⁴⁷ with a time step of 0.25 fs. The equilibration period lasted for 60 ps.

The equilibration step yielded a set of solute-solvent structures in which the solvent was in equilibrium with the solute. These were subsequently employed as the basis for the calculation of the photoabsorption spectrum using the semiclassical nuclear ensemble method.^{48,49} Afterwards, phase space points with excitation energies in the range of 4.0 ± 0.1 eV, which covers the peak of the first

photoabsorption band of compound **II** in water. A set of 25 phase space points were sampled in this manner, and each was used as the starting point for a single FSSH trajectory. In all of these phase space points, the system was occupying the S_1 adiabatic state. The trajectories were propagated until deactivation to the S_0 state, or until the maximum simulation time of 500 fs had elapsed, whichever occurred first.

S4.4.3 Nonadiabatic Molecular Dynamics

The nonadiabatic molecular dynamics simulations were carried out with the fewest switches surface hopping (FSSH) algorithm, adapted for use with the QM/MM method. The FSSH algorithm was implemented in a “wrapper” program which called Turbomole for the calculation of the electronic structure of the solute, then parsed the output, performed the MM part of the calculation, and propagated the equations of motion. Except where noted otherwise, the simulation parameters were the same as in the gas-phase FSSH simulations.

The calculation of the vertical excitation spectrum of compound **II** in aqueous solution (represented by the COSMO model) shows that the S_3 state and all higher singlet states are well separated in energy from the S_1 and S_2 states. Accordingly, only the S_1 and S_2 states were included in the linear expansion of the electronic wavefunction:

$$\Phi(\mathbf{r}, t; \mathbf{R}) = \sum_j a_j(t) \phi_j(\mathbf{r}; \mathbf{R}) \quad (10)$$

The time-evolution of the wavefunction expansion coefficients (equation 11 below) was integrated with the use of the Runge-Kutta fourth-order method with a time step of 0.0004 fs, using quantities interpolated linearly between successive classical steps.

$$i\hbar \dot{a}_k = \sum_j a_j (\delta_{jk} E_k(\mathbf{R}) - i\hbar C_{kj}) \quad (11)$$

In analogy to the gas-phase simulations, for the purpose of calculating the nonadiabatic coupling element (NACME) between the S_1 and S_2 states, the ADC(2) excited-state wavefunctions ϕ_j were approximated as wavefunctions of the configuration interaction singles (CIS) type:

$$|\phi_j\rangle \approx \sum_{i,a} R_i^a |\Phi_i^a\rangle \quad \text{where} \quad |\Phi_i^a\rangle = \hat{a}^\dagger \hat{i} |\Phi_0\rangle \quad (12)$$

Here, Φ_0 is the RHF reference determinant, and R_i^a are elements of the Jacobian eigenvector corresponding to single excitations. The singles excitations part of the Jacobian eigenvector for each state was extracted from Turbomole output files with the use of the program ‘bin2matrix’ distributed as part of the simulation package Newton-X.^{50–53} Subsequently, the NACME was calculated using a finite differences formula:⁵⁴

$$C_{ij}(t + \Delta/2) = \frac{1}{2\Delta} \left[\langle \phi_i(t) | \phi_j(t + \Delta) \rangle - \langle \phi_i(t + \Delta) | \phi_j(t) \rangle \right] \quad (13)$$

Here, Δ is the length of the classical time step (the time step used in the integration of Newton’s equations of motion). The wavefunction overlap terms which appear in

equation 13 were evaluated with the use of the wavefunction overlap program of Plasser and coworkers.^{55,56}

The phases of electronic wavefunctions calculated by a quantum chemistry program such as Turbomole are set arbitrarily, and they can change from one timestep to another. In order to correct for this effect, the wavefunction phases were tracked by calculating overlap elements between electronic states at successive time steps: $\langle \phi_j(t + \Delta) | \phi_j(t) \rangle$. When a phase change was detected, the overlap elements involving the given electronic state were multiplied by -1 .

When the system underwent a nonadiabatic transition (or, ‘hop’) from one state to another, only the velocities of the QM atoms (i.e., atoms comprising the inner subsystem) were rescaled. This measure prevents an unphysical transfer of energy between the inner and outer subsystems.

Once a simulation trajectory had approached the S_1/S_0 crossing seam, such that the energy gap between these states dropped to below 0.25 eV, the system was considered to have undergone internal conversion to the ground state. The trajectory was then discontinued.

S4.4.4 Results and Discussion

Having outlined our implementation of the QM/MM method, we are now prepared to examine the simulation results. We begin by discussing the photoabsorption spectrum of compound **II** in TIP3P/Fs water, which is plotted in Figure S13 (a). Additionally, in Figure S13 (b), the photoabsorption spectrum is broken down into contributions from transitions into the individual adiabatic excited states.

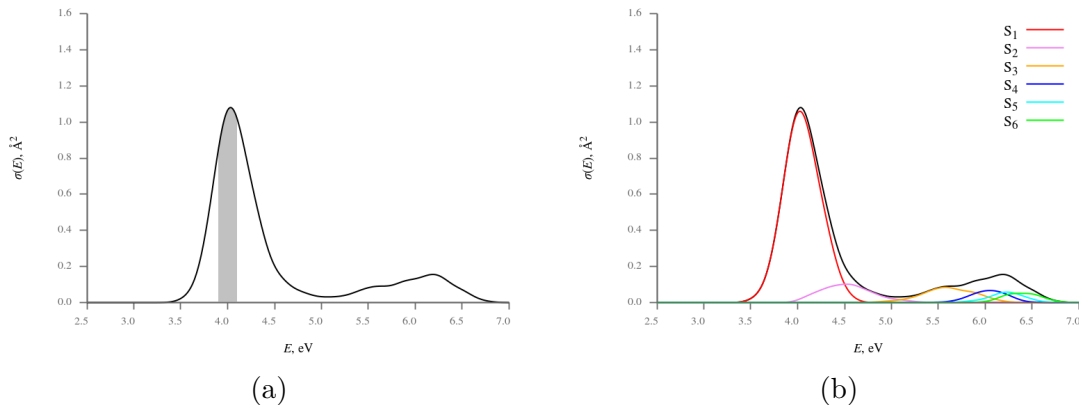
Aqueous solvation causes a blue-shift of the first photoabsorption band, which arises mainly from the $S_0 \rightarrow S_1$ (2^1A) transition. Whereas in the gas phase (Figure 5 (a) in the main body of this paper), this band peaks at a photon energy of 3.79 eV, in aqueous solution the band maximum is found at 4.03 eV. Thus, according in the QM/MM simulation, the blue shift of the band maximum is 0.24 eV. This is consistent with the results obtained with the COSMO implicit solvation model, according to which aqueous solvation causes a slight blue-shift in the vertical excitation energy into the S_1 (2^1A) state (see Section S4.1 above).

The S_2 (1^1B) state is more strongly blue shifted by aqueous solvation than is the S_1 (2^1A) state. As a consequence, in aqueous solution the S_1 and S_2 states are fairly well separated in energy, and there appears to be relatively little intermixing of 2^1A and 1^1B diabatic character.

Figure S14 characterizes the time-evolution of the system following photoexcitation by plotting the classical populations of the adiabatic states S_0 , S_1 , and S_2 and the parameters $\bar{\mu}_{0n}$, α , and τ introduced in the main body of the present work. To briefly recapitulate, parameter $\bar{\mu}_{0n}$ quantifies the transition dipole moment of the occupied state in the ensemble of surviving trajectories; see Section 2.2 in the main body of this paper for details. α is the angle formed by the C5–C6 bond, and the plane defined by atoms C6, N7 and N10. τ is the average of the dihedral angles C1–C5–C6–N7 and C4–C5–C6–N10. When calculating the classical populations of the adiabatic states S_0 to S_2 , those trajectories that had been terminated were counted towards the classical population of the S_0 state.

Overall, the relaxation mechanism of compound **II** in TIP3P/Fs water is analogous to the case of the isolated molecule (see Section 3.4 of the main body of

Figure S13: (a) Simulated photoabsorption spectrum of compound **II** in aqueous solution simulated with the use of the QM/MM method. The shaded area represents the energy interval from which initial conditions for the nonadiabatic molecular dynamics simulations were sampled. (b) Breakdown of the spectrum into contributions from individual adiabatic states.



this paper). Following the initial photoexcitation, the molecule undergoes a bending of the molecular skeleton, which is usually accompanied by intramolecular rotation around the central C5–C6 bond. The return to the ground state proceeds via internal conversion at the S_1/S_0 crossing seam.

For the most part, the simulated trajectories remained in the S_1 state until the moment that they approached the crossing with the S_0 state. The S_2 was populated only sporadically, for up to around ten femtoseconds at a time.

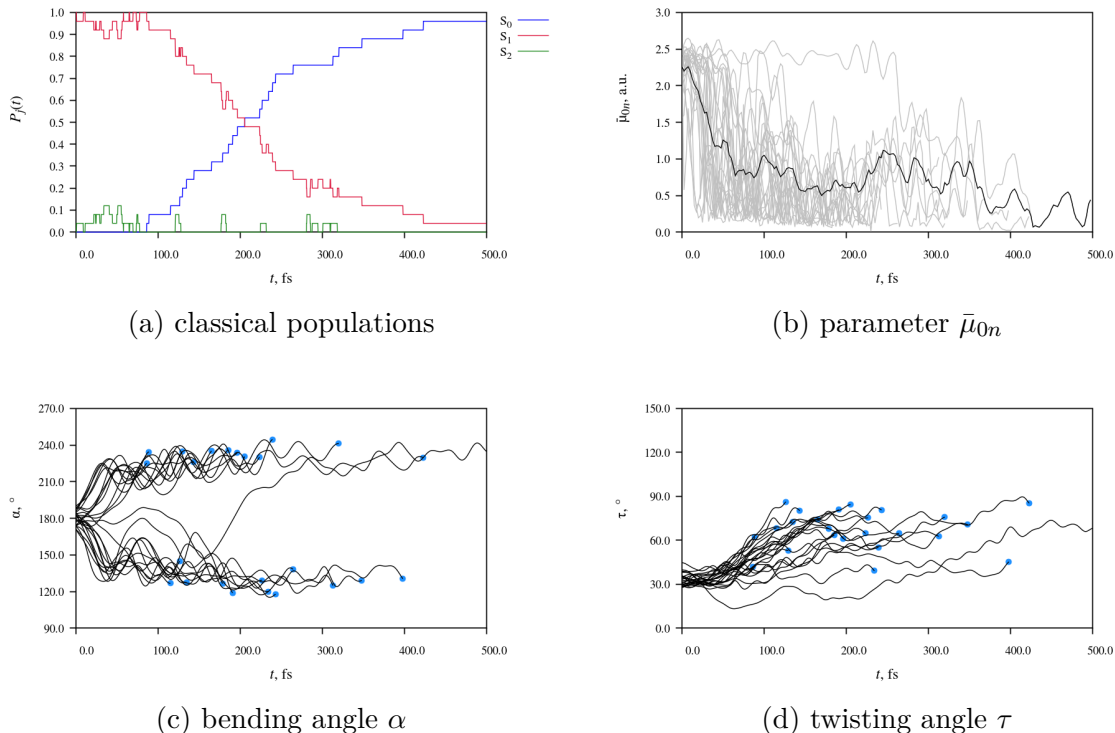
The excited-state lifetime of the compound **II** in aqueous solution is somewhat longer than in the isolated molecule. Whereas in the case of the isolated molecule, the median deactivation time was 92 fs, in aqueous solution it is 205 fs, which is longer by a factor of roughly 2. We attribute the extension of the excited-state lifetime to the destabilization of the region of the PES of the S_1 adiabatic state where it has 1^1B diabatic character with respect to the region where it has 2^1A character. Nevertheless, this effect is relatively minor in absolute terms, and the S_1/S_0 crossing seam remains well accessible also in the solution phase.

All except one of the simulated trajectories deactivated to the S_0 state within the 500 fs time limit. As regards the single trajectory which did not deactivate by $t=500$ fs, there is nothing to suggest that it became permanently trapped in some long-lived excited-state structure. Presumably, if the simulations had been continued beyond $t=500$ fs, that trajectory would have also eventually deactivated to S_0 .

It seems that the presence of the solvent does little to restrain the bending deformation of the molecular skeleton, which is measured by the angle α , or torsion around the central C5–C6 bond, which is measured by the torsional parameter τ . In all of the simulated trajectories, the molecule underwent a pronounced bending deformation within a few tens of femtoseconds after the initial photoexcitation. In most cases, the molecule subsequently remained bent for the remainder of the simulated trajectory. In most of the trajectories, the molecule also underwent intramolecular rotation around the central C5–C6 bond.

Accompanying this narrative, as another part of the Supporting Information we

Figure S14: Time-evolution of electronic structure and molecular geometry during the relaxation dynamics of compound **II** in aqueous solution. Parameter $\bar{\mu}_{0n}$ quantifies the transition dipole moment of the occupied state in the ensemble of trajectories. α is the angle formed by the C5–C6 bond, and the plane defined by atoms C6, N7 and N10. τ is the average of the dihedral angles C1–C5–C6–N7 and C4–C5–C6–N10. In panels (c) and (d), the point in time at which a given trajectory was discontinued is indicated with a blue dot.



provide animations of three representative simulated trajectories. Each animation shows the solute molecule and nearest water molecules around it. (More specifically, the animation shows all water molecules whose oxygen atoms approach the solute molecule to within 4.25 Å at least once during the simulation. The remaining water molecules are hidden from view.) The panel on the bottom shows the energy gaps between the S_1 and S_2 states, and the S_0 state. The passage of time is indicated with a vertical black line moving along the time axis. The currently occupied state is marked with a black circle.

In summary, solvation effects on the photophysics of compound **II** are, on the whole, rather subtle. Although in TIP3P/Fs water, the excited-state lifetime is longer than under isolated-molecule conditions, it is still relatively short. Indeed, all except one of the simulated trajectories have deactivated near the S_1/S_0 crossing seam within 500 fs of the initial photoexcitation. We ascribe this to the fact that relaxation from the Franck-Condon geometry to the S_1/S_0 crossing seam is strongly favoured by the topography of the excited-state PESs. Aqueous solvation causes only a fairly minor alteration of the potential energy landscape, and so the molecule undergoes internal conversion to the ground state through the same relaxation pathway as in the isolated-molecule simulations.

S5 Molecular Geometries

The present section lists selected geometries of compounds **II** and **III**. All geometries are given in terms of Cartesian coordinates in units of ångström (Å).

Ground-state equilibrium geometry (S_0 -min) of compound **II**, as optimized at the MP2/cc-pVDZ level of theory:

N	-0.0953261	-1.0874837	0.4842613
N	0.0953261	1.0874837	0.4842613
C	0.4502539	0.5554107	-3.9524037
C	-0.4502539	-0.5554107	-3.9524037
H	1.4400934	1.6687506	-2.2917752
H	-1.4400934	-1.6687506	-2.2917752
C	0.0000000	0.0000000	-1.7695262
C	0.0827242	2.4705287	0.0286106
C	-0.0827242	-2.4705287	0.0286106
C	0.7188551	0.9164755	-2.6227135
C	-0.7188551	-0.9164755	-2.6227135
C	0.0000000	0.0000000	-0.3500603
C	0.0667576	0.6872511	1.8186925
C	-0.0667576	-0.6872511	1.8186925
C	0.1580379	1.6596583	2.9494773
C	-0.1580379	-1.6596583	2.9494773
H	0.8772053	1.0344280	-4.8380203
H	-0.8772053	-1.0344280	-4.8380203
H	-1.0494455	-2.3025650	2.8532917
H	1.0494455	2.3025650	2.8532917
H	-0.5084473	3.0762340	0.7312505
H	0.5084473	-3.0762340	0.7312505
H	-0.3725268	2.4889456	-0.9724658
H	0.3725268	-2.4889456	-0.9724658
H	1.1039993	2.8787551	-0.0386499
H	-1.1039993	-2.8787551	-0.0386499
H	0.2363777	1.1184412	3.9040688
H	0.7276188	-2.3162064	3.0061690
H	-0.7276188	2.3162064	3.0061690
H	-0.2363777	-1.1184412	3.9040688

Ground-state equilibrium geometry (S_0 -min) of compound **III**, as optimized at the MP2/cc-pVDZ level of theory:

C	0.0000000	0.0000000	-0.6604610
C	0.0000000	0.0000000	0.7431260
H	0.0000000	1.3565700	3.8030460
H	0.0000000	-1.3565700	3.8030460
H	0.0000000	-2.0365760	-1.1611040
H	0.0000000	2.0365760	-1.1611040
H	0.0000000	-1.3950300	-3.6578010
H	0.0000000	1.3950300	-3.6578010
C	0.0000000	-1.1665860	1.5903980
C	0.0000000	1.1665860	1.5903980
C	0.0000000	0.7186740	2.9151540
C	0.0000000	-0.7186740	2.9151540
C	0.0000000	-0.6854890	-2.8349480
C	0.0000000	0.6854890	-2.8349480
N	0.0000000	-1.0822590	-1.5025480
N	0.0000000	1.0822590	-1.5025480
H	0.0000000	-2.2110520	1.2620810
H	0.0000000	2.2110520	1.2620810

Ground-state equilibrium geometry (S_0 -min) of compound **III**, as optimized at the SA-2-CASSCF(12,10)/cc-pVDZ level of theory:

C	-0.6499726	0.0000000	0.0000000
C	0.7228046	0.0000000	0.0000000
H	3.7724363	-1.3523851	0.0000000
H	3.7724363	1.3523851	0.0000000
H	-1.1683378	2.0223881	0.0000000
H	-1.1683378	-2.0223881	0.0000000
H	-3.6344275	1.3748769	0.0000000
H	-3.6344275	-1.3748769	0.0000000
C	1.5918831	1.1627944	0.0000000
C	1.5918831	-1.1627944	0.0000000
C	2.8925217	-0.7259658	0.0000000
C	2.8925217	0.7259658	0.0000000
C	-2.8209412	0.6739037	0.0000000
C	-2.8209412	-0.6739037	0.0000000
N	-1.4884735	1.0813620	0.0000000
N	-1.4884735	-1.0813620	0.0000000
H	1.2744728	2.1961176	0.0000000
H	1.2744728	-2.1961176	0.0000000

Minimum along the S_1/S_0 conical intersection seam (MCI) of compound **III**, as optimized at the SA-2-CASSCF(12,10)/cc-pVDZ level of theory (without the imposition of constraints):

C	0.0000000	0.0000000	0.0000000
C	0.0000000	0.0000000	1.4870212
N	0.0000000	1.2455290	2.1805485
C	-0.5642159	0.9942865	3.4480389
C	-1.1431881	-0.2166970	3.4365124
N	-0.9758354	-0.7921260	2.1569661
H	0.8676617	1.7457742	2.1610041
H	-0.8015593	-1.7790357	2.1302610
H	-0.6030369	1.7584360	4.2057743
H	-1.7707690	-0.6776763	4.1800912
C	1.1367909	0.0457975	-0.8321588
C	0.6981131	0.0454720	-2.2239663
C	-0.6744187	-0.0088057	-2.2295633
C	-1.1285804	-0.0379887	-0.8420095
H	2.1632869	0.0604196	-0.4973071
H	-2.1538708	-0.0832480	-0.5103946
H	1.3485585	0.0782697	-3.0842363
H	-1.3166195	-0.0219496	-3.0967633

Minimum along the S_1/S_0 conical intersection seam (MCI) of compound **III**, reoptimized at the XMS-CASPT2/cc-pVDZ level of theory (without the imposition of constraints):

C	0.0855872	0.0317695	1.5047793
C	0.0523161	0.0431809	0.0177024
H	-1.3541951	0.1168160	-3.0811113
H	1.3299222	-0.1333526	-3.1276086
H	0.6301622	1.9755610	2.1016685
H	-0.6317602	-1.8438637	2.1128125
H	-0.8003530	1.7793213	4.1962112
H	-1.6891520	-0.8236701	4.1895914
C	1.1579927	-0.0848091	-0.8482414
C	-1.0959817	0.1322234	-0.8150454
C	-0.6819809	0.0635664	-2.2228480
C	0.6888609	-0.0607507	-2.2474798
C	-0.6653190	1.0035577	3.4454027
C	-1.1043302	-0.2900034	3.4433019
N	-0.0964726	1.2707928	2.1954553
N	-0.8159078	-0.8462253	2.1884870
H	2.1965535	-0.2004726	-0.5287871
H	-2.1236418	0.2227984	-0.4544805

References

- [1] Bader R. F. W. *Atoms in Molecules. A Quantum Theory*; Oxford University Press: Oxford, UK, 1990.
- [2] Matta, C. F.; Boyd, R. J. An Introduction to the Quantum Theory of Atoms in Molecules. In *The Quantum Theory of Atoms in Molecules*; Matta, C. F.; Boyd, R. J., Eds.; Wiley-VCH: Weinheim, Germany, 2007; pp 1-34.
- [3] Gaussian 09, Revision D.01, Frisch, M. J.; Trucks, G. W.; Schlegel, H. B.; Scuseria, G. E.; Robb, M. A.; Cheeseman, J. R.; Scalmani, G.; Barone, V.; Mennucci, B.; Petersson, G. A. et al., Gaussian, Inc., Wallingford CT, 2009.
- [4] Lu, T.; Chen, F. Multiwfn: A Multifunctional Wavefunction Analyzer. *J. Comput. Chem.* **2012**, *33*, 580-592. DOI: 10.1002/jcc.22885
- [5] Multiwfn homepage: sobereva.com/multiwfn/
- [6] Harder, S. Can C–H \cdots C(π) Bonding Be Classified as Hydrogen Bonding? A Systematic Investigation of C–H \cdots C(π) Bonding to Cyclopentadienyl Anions. *Chem. Eur. J.* **1999**, *5*, 1852-1861. DOI: 10.1002/(SICI)1521-3765(19990604)5:6<1852::AID-CHEM1852>3.0.CO;2-I
- [7] Abernethy, C. D.; Macdonald, C. L. B.; Clyburne, J. A. C.; Cowley, A. H. A Persistent C–H \cdots C(π) T-Stacked Cation. *Chem. Commun.* **2001**, 61-62. DOI: 10.1039/b005450j
- [8] Madura, I. D.; Zachara, J.; Leszczyńska, K.; Kunicki, A. R. Crystal Structure of Dicyclopentadienylaluminum Complex Directed by Weak C–H \cdots π Interactions. *J. Mol. Struct.* **2010**, *968*, 93-98. DOI: 10.1016/j.molstruc.2010.01.029
- [9] Grabowski, S. J.; Lipkowski, P. Characteristics of X–H \cdots π Interactions: Ab Initio and QTAIM Studies. *J. Phys. Chem. A* **2011**, *115*, 4765-4773. DOI: 10.1021/jp2005327
- [10] Chen, Z.; Wannere, C. S.; Corminboeuf, C.; Puchta, R.; Schleyer, P. v. R. Nucleus-Independent Chemical Shifts (NICS) as an Aromaticity Criterion. *Chem. Rev.* **2005**, *105*, 3842-3888. DOI: 10.1021/cr030088+
- [11] London, F. Théorie Quantique des Courants Interatomiques dans les Combinaisons Aromatiques. *J. Phys. Radium* **1937**, *8*, 397-408. DOI: 10.1051/jphysrad:01937008010039700
- [12] McWeeny, R. Perturbation Theory for Fock-Dirac Density Matrix. *Phys. Rev.* **1962**, *126*, 1028-1034. DOI: 10.1103/PhysRev.126.1028
- [13] Ditchfield, R. Self-Consistent Perturbation Theory of Diamagnetism. 1. Gauge-Invariant LCAO Method for N.M.R. Chemical Shifts. *Mol. Phys.* **1974**, *27*, 789-807. DOI: 10.1080/00268977400100711

- [14] Wolinski, K.; Hilton, J. F.; Pulay, P. Efficient Implementation of the Gauge-Independent Atomic Orbital Method for NMR Chemical Shift Calculations. *J. Am. Chem. Soc.* **1990**, *112*, 8251-8260. DOI: 10.1021/ja00179a005
- [15] Cheeseman, J. R.; Trucks, G. W.; Keith, T. A.; Frich, M. J. A Comparison of Models for Calculating Nuclear Magnetic Resonance Shielding Tensors. *J. Chem. Phys.* **1996**, *104*, 5497-5509. DOI: 10.1063/1.471789
- [16] Dsouza, R.; Cheng, X.; Li, Z.; Miller, R. J. D.; Kochman, M. A. Oscillatory Photoelectron Signal of *N*-Methylmorpholine as a Test Case for the Algebraic-Diagrammatic Construction Method of Second Order *J. Phys. Chem. A* **2018**, *122*, 9688-9700. DOI: 10.1021/acs.jpca.8b10241
- [17] Christiansen, O.; Koch, H.; Jørgensen, P. The Second-Order Approximate Coupled Cluster Singles and Doubles Model CC2 *Chem. Phys. Lett.* **1995**, *243*, 409-418, DOI: 10.1016/0009-2614(95)00841-Q
- [18] Hättig, C. Structure Optimizations for Excited States with Correlated Second-Order Methods: CC2 and ADC(2). In *Advances in Quantum Chemistry*; Jensen, H. J. Å., Ed.; Academic Press: New York, 2005; Vol. 50; pp 37-60. DOI: 10.1016/S0065-3276(05)50003-0
- [19] Hohenstein, E. G.; Kokkila, S. I. L.; Parrish, R. M.; Martínez, T. J. Tensor Hypercontraction Equation-of-Motion Second-Order Approximate Coupled Cluster: Electronic Excitation Energies in $\mathcal{O}(N^4)$ Time *J. Phys. Chem. B* **2013**, *117*, 12972-12978, DOI: 10.1021/jp4021905
- [20] Szalay, P. G.; Watson, T.; Perera, A.; Lotrich, V. F.; Bartlett, R. J. Benchmark Studies on the Building Blocks of DNA. 1. Superiority of Coupled Cluster Methods in Describing the Excited States of Nucleobases in the Franck-Condon Region *J. Phys. Chem. A* **2012**, *116*, 6702-6710, DOI: 10.1021/jp300977a.
- [21] Tajti, A.; Szalay, P. G. Investigation of the Impact of Different Terms in the Second Order Hamiltonian on Excitation Energies of Valence and Rydberg States *J. Chem. Theory Comput.* **2016**, *12*, 5477-5482. DOI: 10.1021/acs.jctc.6b00723
- [22] Zhao, Y.; Truhlar, D. G. The M06 Suite of Density Functionals for Main Group Thermochemistry, Thermochemical Kinetics, Noncovalent Interactions, Excited States, and Transition Elements: Two New Functionals and Systematic Testing of Four M06-Class Functionals And 12 Other Functionals *Theor. Chem. Account* **2008**, *120*, 215-241. DOI: 10.1007/s00214-007-0310-x
- [23] Weigend, F.; Ahlrichs, R. Balanced Basis Sets of Split Valence, Triple Zeta Valence and Quadruple Zeta Valence Quality for H to Rn: Design and Assessment of Accuracy *Phys. Chem. Chem. Phys.* **2005**, *7*, 3297-3305. DOI: 10.1039/B508541A
- [24] Koopmans, T. Über die Zuordnung von Wellenfunktionen und Eigenwerten zu den Einzelnen Elektronen Eines Atoms. *Physica* **1934**, *1*, 104-113. DOI: 10.1016/S0031-8914(34)90011-2

- [25] Klamt, A.; Schüürmann, G. COSMO: A New Approach to Dielectric Screening in Solvents with Explicit. Expressions for the Screening Energy and its Gradient *J. Chem. Soc., Perkin Trans. 2*, **1993**, 799-805.
- [26] Lunkenheimer, B.; Köhn, A. Solvent Effects on Electronically Excited States Using the Conductor-Like Screening Model and the Second-Order Correlated Method ADC(2) *J. Chem. Theory Comput.* **2013**, 9, 977-994.
- [27] TURBOMOLE V7.0 2015, a development of University of Karlsruhe and Forschungszentrum Karlsruhe GmbH, 1989-2007, TURBOMOLE GmbH, since 2007; available from <http://www.turbomole.com>.
- [28] Politzer, P.; Laurence, P. R.; Jayasuriya, K. Molecular Electrostatic Potentials: an Effective Tool for the Elucidation of Biochemical Phenomena. *Environ. Health Perspect.* **1985**, 61, 191-202. DOI: 10.1289/ehp.8561191
- [29] Politzer, P.; Murray, J. S. The Fundamental Nature and Role of the Electrostatic Potential in Atoms and Molecules. *Theor. Chem. Acc.* **2002**, 108, 134-142. DOI: 10.1007/s00214-002-0363-9
- [30] Jeziorski, B.; Moszynski, R.; Szalewicz, K. Perturbation Theory Approach to Intermolecular Potential Energy Surfaces of van der Waals Complexes *Chem. Rev.* **1994**, 94, 1887-1930. DOI: 10.1021/cr00031a008
- [31] Stone, A. J. The Theory of Intermolecular Forces, 2nd ed.; Oxford University Press: Oxford, 2013.
- [32] Hummer, G. Electrostatic Potential of a Homogeneously Charged Square and Cube in Two and Three Dimensions arXiv:chem-ph/9508002
- [33] Hummer, G. Electrostatic Potential of a Homogeneously Charged Square and Cube in Two and Three Dimensions *Journal of Electrostatics* **1996**, 36, 285-291. DOI: 10.1016/0304-3886(95)00052-6
- [34] Friesner, R. A.; Guallar, V. Ab Initio Quantum Chemical and Mixed Quantum Mechanics/Molecular Mechanics (QM/MM) Methods for Studying Enzymatic Catalysis. *Annu. Rev. Phys. Chem.* **2005**, 56, 389-427. DOI: 10.1146/annurev.physchem.55.091602.094410
- [35] Lin, H.; Truhlar, D. G. QM/MM: What Have We Learned, Where Are We, and Where Do We Go From Here? *Theor. Chem. Acc.* **2007**, 117, 185-199. DOI: 10.1007/s00214-006-0143-z
- [36] Senn, H. M.; Thiel, W. QM/MM Methods for Biological Systems. *Top. Curr. Chem.* **2007**, 268, 173-290. DOI: 10.1007/128_2006_084
- [37] Jorgensen, W. L.; Maxwell, D. S.; Tirado-Rives, J. Development and Testing of the OPLS All-Atom Force Field on Conformational Energetics and Properties of Organic Liquids. *J. Am. Chem. Soc.* **1996**, 118, 11225-11236. DOI: 10.1021/ja9621760

- [38] Schmitt, U. W.; Voth, G. A. The Computer Simulation of Proton Transport in Water. *J. Chem. Phys.* **1999**, *111*, 9361-9381. DOI: 10.1063/1.480032
- [39] Ruckebauer, M.; Barbatti, M.; Müller, T.; Lischka, H. Nonadiabatic Excited-State Dynamics with Hybrid *ab Initio* Quantum-Mechanical/Molecular-Mechanical Methods: Solvation of the Pentadieniminium Cation in Apolar Media *J. Phys. Chem. A* **2010**, *114*, 6757-6765. DOI: 10.1021/jp103101t
- [40] Ruckebauer, M.; Barbatti, M.; Müller, T.; Lischka, H. Nonadiabatic Photodynamics of a Retinal Model in Polar and Nonpolar Environment *J. Phys. Chem. A* **2013**, *117*, 2790-2799. DOI: 10.1021/jp400401f
- [41] Barbatti, M.; Kakali, S. Effects of Different Initial Condition Samplings on Photodynamics and Spectrum of Pyrrole. *Int. J. Quantum Chem.* **2016**, *116*, 762-771. DOI: 10.1002/qua.25049
- [42] Bowman, J. M.; Gazdy, B.; Sun, Q. A Method to Constrain Vibrational Energy in Quasiclassical Trajectory Calculations *J. Chem. Phys.* **1989**, *91*, 2859-2862. DOI: 10.1063/1.456955
- [43] Guo, Y.; Thompson, D. L.; Sewell, T. D. Analysis of the Zero-Point Energy Problem in Classical Trajectory Simulations *J. Chem. Phys.* **1996**, *104*, 576-582. DOI: 10.1063/1.470853
- [44] Martínez-Fernández, L.; Corral, I.; Granucci, G.; Persico, M. Competing Ultrafast Intersystem Crossing and Internal Conversion: A Time Resolved Picture for the Deactivation of 6-Thioguanine. *Chem. Sci.* **2014**, *5*, 1336-1347. DOI: 10.1039/c3sc52856a
- [45] Singh, U. C.; Kollman, P. A. An Approach to Computing Electrostatic Charges for Molecules. *J. Comp. Chem.* **1984**, *5*, 129-145. DOI: 10.1002/jcc.540050204
- [46] Gaussian 16, Revision B.01, Frisch, M. J.; Trucks, G. W.; Schlegel, H. B.; Scuseria, G. E.; Robb, M. A.; Cheeseman, J. R.; Scalmani, G.; Barone, V.; Mennucci, B.; Petersson, G. A. et al., Gaussian, Inc., Wallingford CT, 2016.
- [47] Brünger, A.; Brooks III, C. L.; Karplus, M. Stochastic Boundary Conditions for Molecular Dynamics Simulations of ST2 Water. *Chem. Phys. Lett.* **1984**, *105*, 495-500. DOI: 10.1016/0009-2614(84)80098-6
- [48] Barbatti, M.; Aquino, A. J. A.; Lischka, H. The UV absorption of Nucleobases: Semi-Classical *Ab Initio* Spectra Simulations. *Phys. Chem. Chem. Phys.* **2010**, *12*, 4959-4967. DOI: 10.1039/B924956G
- [49] Crespo-Otero, R.; Barbatti, M. Spectrum Simulation and Decomposition with Nuclear Ensemble: Formal Derivation and Application to Benzene, Furan and 2-Phenylfuran. *Theor. Chem. Acc.* **2012**, *131*, 1237. DOI: 10.1007/s00214-012-1237-4
- [50] Barbatti, M.; Granucci, G.; Ruckebauer, M.; Plasser, F.; Crespo-Otero, R.; Pittner, J.; Persico, M.; Lischka, H. NEWTON-X: a package for Newtonian dynamics close to the crossing seam, version 2.0, www.newtonx.org (2017).

- [51] Plasser, F.; Crespo-Otero, R.; Pederzoli, M.; Pittner, J.; Lischka, H.; Barbatti, M. Surface Hopping Dynamics with Correlated Single-Reference Methods: 9H-Adenine as a Case Study. *J. Chem. Theory Comput.* **2014**, *10*, 1395-1405. DOI: 10.1021/ct4011079
- [52] Barbatti, M.; Granucci, G.; Persico, M.; Ruckebauer, M.; Vazdar, M.; Eckert-Maksic, M.; Lischka, H. The On-the-Fly Surface-Hopping Program System Newton-X: Application to *Ab Initio* Simulation of the Nonadiabatic Photodynamics of Benchmark Systems. *J. Photochem. Photobiol., A* **2007**, *190*, 228-240. DOI: 10.1016/j.jphotochem.2006.12.008
- [53] Barbatti, M.; Ruckebauer, M.; Plasser, F.; Pittner, J.; Granucci, G.; Persico, M.; Lischka, H. Newton-X: a Surface-Hopping Program for Nonadiabatic Molecular Dynamics. *Wiley Interdiscip. Rev.: Comput. Mol. Sci.* **2014**, *4*, 26-33. DOI: 10.1002/wcms.1158
- [54] Tavernelli, I.; Tapavicza, E.; Rothlisberger, U. Nonadiabatic Coupling Vectors Within Linear Response Time-Dependent Density Functional Theory. *J. Chem. Phys.* **2009**, *130*, 124107. DOI: 10.1063/1.3097192
- [55] Plasser, F.; Ruckebauer, M.; Mai, S.; Oppel, M.; Marquetand, P.; González, L. Efficient and Flexible Computation of Many-Electron Wavefunction Overlaps. *J. Chem. Theory Comput.* **2016**, *12*, 1207-1219. DOI: 10.1021/acs.jctc.5b01148
- [56] Plasser, F.; González, L. Communication: Unambiguous Comparison of Many-Electron Wavefunctions Through Their Overlaps *J. Chem. Phys.* **2003**, *118*, 021103. DOI: 10.1063/1.4958462